IEEE Access
Multidisciplinary | Rapid Review | Open Access Journal

Received November 24, 2020, accepted December 12, 2020, date of publication December 16, 2020,
date of current version December 31, 2020.

*Digital Object Identifier 10.1109/ACCESS.2020.3045344*

# A Novel Hyperbolic Tangent Profile for Optical Fiber for Next Generation OAM-MDM Systems

**ALAAEDDINE RJEB[1], HABIB FATHALLAH[2], (Senior Member, IEEE), ISSA KHALED[1], MOHSEN MACHHOUT[1], AND SALEH A. ALSHEBEILI[3], (Member, IEEE)**

[1]Laboratory of Electronics and Micro-Electronics, Department of Physics, Faculty of Sciences of Monastir, University of Monastir, Monastir 5019, Tunisia
[2]Laboratory of Artificial Intelligence and Data Engineering Applications, Computer Department, Faculty of Sciences of Bizerte, University of Carthage, Tunis 1054, Tunisia
[3]Electrical Engineering Department, King Saud University, Riyadh 11421, Saudi Arabia

Corresponding author: Alaaeddine Rjeb (alaaeddine.rjeb@gmail.com)

This work was supported by the King Saud University, Riyadh, Saudi Arabia, through the Researchers Supporting Project, under Grant RSP-2020/46.

**ABSTRACT** In this work, we propose and theoretically/numerically investigate a novel parametric refractive index profile for few mode fibers, referred to as a hyperbolic tangent few mode fiber (HTAN-FMF). To the best of our knowledge, the HTAN-FMF is adopted for the first time, to simultaneously maximize the inter-channels separation and OAM purity. The proposed FMF achieves a wide separation between cylindrical vector modes ($\geq 3 \times 10^{-4}$ between $TE_{0,1}$, $HE_{2,1}$, and $TM_{0,1}$). This enables low-level crosstalk and clearly overcomes recently reported levels in literature. On the other hand, simulations show that the generated and evaluated OAM modes are mostly high pure ($\geq$ 99.9%) leading to intrinsic crosstalk as minimum as -30 dB during propagation through HTAN-FMF. Other propagation performance metrics of the proposed fiber including chromatic dispersion and differential mode delay are also evaluated over the C ITU-T band showing that HTAN-FMF has the potential to achieve stable OAM modes transmission. Bending insensitivity is numerically proved showing that the proposed FMF has the potential to enhance the transmission capacity and the spectral efficiency in next generation OAM mode division Multiplexing (OAM-MDM) systems.

**INDEX TERMS** Space division multiplexing, few mode fiber design, orbital angular momentum.

## I. INTRODUCTION

During last years, the unprecedented explosion in data traffic caused by the colossal progress in social networking, the cloud computing, and big data applications, put pressure on telecommunications community to develop higher capacity optical networks [1], [2].

Space division multiplexing (SDM) has gained a widespread popularity due to its capability to overcome the capacity crunch of already deployed single mode fiber (SMF) [3]. SDM has the advantage of increasing the number of data channels available inside an optical fiber. An attractive embodiment of SDM is the mode division multiplexing (MDM) based on excitation and propagation of several optical modes within few mode fibers (FMF). Often, FMF uses linear polarized modes (LP) as a mode basis carrying data. Heavy and complex ''multiple input multiple output'' digital signal processing (MIMO DSP) is required at the fiber end (receiver) to lift the degeneracy of propagating LP modes since they are formed by a superposition of several degenerate and polarization vector modes. The complexity of MIMO DSP increases as the number of propagating LP modes increases [4], [5].

Orbital angular momentum (OAM), also known as twisted light, is arguably one of the most promising approaches that has recently received special attention in both: free space and optical fiber networks. In fact, OAM is known by the unboundedness and the orthogonality among the co-propagating modes (channels) [6]. This will make a breakthrough in optical communication.

interestingly, OAM modes have proved its effectiveness in Terabit to Petabit scale capacity transmission and unleashed from dozen to hundred (bit/s/Hz) spectral efficiency over free space communication link [7]. Recalling here that FSO links

The associate editor coordinating the review of this manuscript and approving it for publication was Md Selim Habib.

are much appropriate when the optical fiber deployment is costly or not applicable. It has been demonstrated that carrying data on Laguerre–Gaussian beams (LG), incorporating two degrees of freedom (i.e. with various azimuthal indices and nonzero radial indices), has shown a great capability to enhance free-space system capacity and spectral efficiency. On the other hand, FSO based OAM modes faces several challenges where atmospheric turbulence (AT) is the main of them. AT leads to wavefront distortion and beam spreading & wandering where several techniques have been performed to mitigate AT effects including adaptive optics and low-density parity-check coding [8].

Considering the future of optical fiber communication, OAM modes may possibly look to replace the classic LP modes in new generation optical fibers. Special fibers proposed, designed, and manufactured, to support OAM modes transmission are referred to as OAM-fibers. Three main common features between these special optical fibers are identified. The first feature is the high contrast between core and cladding refractive indices, which increases the mode effective indices separation ($\Delta n_{eff}$), hence enables low induced crosstalk. The second feature is pertaining to the refractive index that matches the donut shape of OAM mode intensity (Ring shape). Finally, the interfaces (core/cladding) are smoothed (instead of being in a step form) in order to eliminate the spin-orbit-coupling inducing mode purity impairment [9]–[21].

Targeting these design recommendations, Ramachandran *et al.* have reported a vortex fiber (VF) having $\Delta n_{eff} = 1.8 \times 10^{-4}$ between cylindrical vector modes [9]. Subsequently, the same team reported the transmission of two OAM states over 1.1 km vortex fiber, reaching terabit scale in capacity transmission [10].

Hollow (air) core fiber has been reported in [11] and [12]. In [11], the fiber (supporting 12 OAM states) is characterized by a good separation among its supported vector modes ($\Delta n_{eff} = 1 \times 10^{-4}$). In [12], 17 OAM states equivalent to 36 information channels, have been demonstrated over air core fiber (ACF). Recently, a free MIMO 10.56 Tbit/s has been demonstrated over 1.2 km ACF by carrying data over 12 OAM modes combined with wavelength division multiplexing (WDM) [13]. Latest air core ring fiber is designed to support more than 1000 OAM modes (using $As_2S_3$ as ring material ) across wide wavelength band covering S, O, E, S, C, and L Bands [14].

On the other hand, the general ring shape has been applied considering both step and graded refractive index profiles. In one side, step ring core fiber (RCF) has been investigated in the context of OAM transmission demonstrating good features in terms of effective index separation and dispersion [15]. Recently, 50 OAM states divided into 13 mode groups (MGs) have been numerically investigated in RCF using small MIMO DSP blocks [16]. Experimentally, a 50 km ring core fiber transmission over two OAM mode-group is demonstrated without MIMO DSP [17].

On the other side, graded index ring core fiber (GIRCF) is a nascent kind of OAM fiber that has been reported and shown to have capability to alleviate the spin-orbit coupling [18].Recently, using two OAM modes and 112 Wavelength channels (WDM), 8.4 Tbit/s has been reached using GIRCF [19].

Recently, we have proposed inverse raised cosine fiber (IRC-FMF) for OAM mode transmission that has shown great capability to lift modal degeneracies [20]. One particularly attractive profile is known as inverse parabolic graded index fiber IPGIF [21], characterized by an inner "smooth" gradient profile controlled by shape parameter $N$ and outer Sharpe index behavior. with this heterogeneous structure-mixture, this profile ensures large effective indices separation among its supported cylindrical vector modes ($>2.1 \times 10^{-4}$). The transmission of eight OAM states over 1 m and two OAM states over more than 1 km have been experimentally demonstrated; thus, making the IPGI fiber suitable for both short and long-distance OAM based multiplexing system. In 2017, the multiplexing/transmission and demultiplexing of 3.36 Tbit/s have been demonstrated over 10-meters inverse parabolic graded index fiber using four OAM modes and 15 wavelengths [22].

The race is ongoing and it is still quite challenging to find the appropriate refractive index profile for optical fiber that both supports high number of OAM states while keeping the inter channels crosstalk very low. other performance metrics are also critical to ensure a robust OAM mode transmission including chromatic dispersion, differential group delay, OAM mode purity and intrinsic crosstalk. Moreover, given the huge demonstrated data capacity in these OAM-fibers categories, it is essential to examine the fibers under practical environment (bending, twist, and ellipticity, etc) which could both direct the design (as well as the optimization) process and contribute to progress from prototyping (in labs) to commercialization and then to deployment (FTTH: Fiber To The Home).

Motivated by the promising results above, we propose and theoretically/numerically examine a novel parametric refractive index profile for FMF (referred to Hyperbolic Tangent FMF: HTAN−FMF). This aims to ensure wider effective indices separation among the supported cylindrical vector modes. To the best of our knowledge, the hyperbolic tangent function has never been used as an optical fiber profile. Similar to graded index function, HTAN has a shape factor ($\alpha$) that controls the shape of the index variation.

After analyzing the generic parameters of HTAN fiber (Section II), in Section III, we investigate the impact of the profile parameters on intermodal separation. Aiming to find the optimum parameters for wider separation, the investigation was carried out using a theoretical approach validated by a numerical simulation using finite element method (FEM). Once achieved, the OAM modes are generated and assessed in terms of purity and intrinsic crosstalk (Section IV). A full OAM mode analysis was performed over wavelength including the chromatic dispersion and the differential group delay.

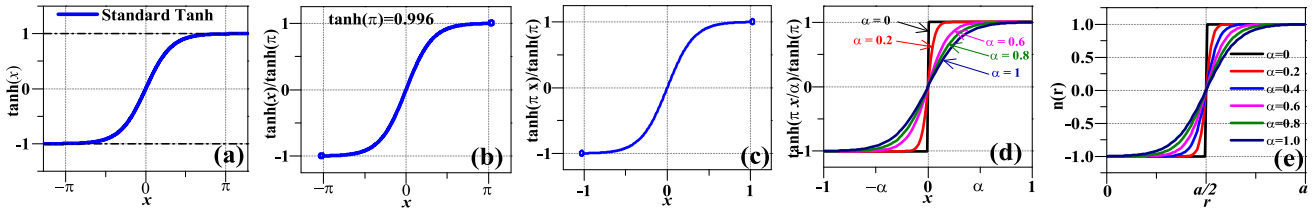


**FIGURE 1.** (a) Standard hyperbolic tangent function tanh, (b) truncated tanh, (c) scaled tanh, (d) modified tanh for different values of shape parameter $\alpha$, and (e) the shifted tanh function for different values of $\alpha$.

Finally, the effects of tight bend on the intermodal separation, on OAM quality, and on modal confinement are investigated (Section V). Section VI provides conclusions and some future research perspectives.

## II. HYPERBOLIC TANGENT PROFILE DESCRIPTION AND DESIGN GUIDELINES

As reported in [21], the idea of designing a refractive index profile that is adapted to OAM transmission is driven by the need to achieve a wide separation between supported cylindrical vector modes. In principle, this is achievable when the index profile fulfills both criteria: (1) high-refractive-index contrast between the core and the cladding, and (2) sharp index change at the core-cladding boundary. Fortunately, both criteria are intrinsic characteristics of our proposed profile. We refer to the later as modified hyperbolic tangent profile (HTAN). This is widely used in various fields/domains such as digital neural networks [23], image processing [24], digital filters [25], and decoding algorithms [26] but not common in waveguide and optical fiber designs.

The standard hyperbolic tangent function (Fig. 1 (a)) is an odd function ($\tanh(-r) = -\tanh(r)$) given by $\tanh(r) = (e^{r}-e^{-r})/(e^{r}+e^{-r})$, defined from $-\infty$ to $+\infty$, which monotonically increases from $-1$ to 1 (Fig. 1(a)). Since the standard tanh function is defined over an infinite real interval, it could not be used directly for fiber index profile because of its limited/realistic extent. This leads to a truncation operation of tanh in a way that keeps only its central part where the most of the change occurs between both levels (minimum and maximum). This truncation limits the extent of the function to an interval that is shorter than $[-1, 1]$.

We normalize the tanh function by $\tanh(\pi)$, since 99.6% of maximum is reached at this point. Our target is to normalize ( see Fig. 1 (b)) and scale the standard function between $[-1, 1]$. This is achievable by considering $\tanh(\pi x)/\tanh(\pi)$; see Fig. 1(c). We introduce a shaping parameter "$\alpha$" where $\alpha \in [0, 1]$ in order to enable adjusting (control the slope) the smoothing level of the obtained tanh function (Figure 1 (d)). The resulting function is written as $\tanh(\frac{\pi x}{\alpha})/\tanh(\pi))$ for $-\alpha \leq x \leq \alpha$.

Moving to transpose the function into the fiber dimension, where $r$ is the distance from core center to the cladding and $a$ is the core radius, we make a variable change where $-\alpha \leq x \leq \alpha$ is substituted by $-\alpha\frac{a}{2} \leq r \leq \alpha\frac{a}{2}$. The resulting function is written as $\tanh[(\pi x)/(\alpha a/2)]/\tanh(\pi)$.

We then shift the function from the origin to $r = a/2$. The shifted function becomes: $n(r) = tanh[\frac{\pi}{\alpha}(\frac{r-a/2}{a/2})]/tanh(\pi)$ for $a(1-\alpha)/2 \leq r \leq a(1+\alpha)/2$, (see Fig 1(e)) where $a(1+\alpha)/2$ is the truncated inner core radius. Considering the full space $[-\infty + \infty]$, the final function is written as:

$$n(r) = \begin{cases} 1 & if\ 0 \leq |r| \leq a\dfrac{1-\alpha}{2} \\ tanh\left[\dfrac{\pi}{\alpha}\dfrac{(r-\frac{a}{2})}{\frac{a}{2}}\right] & if\ a\dfrac{1-\alpha}{2} \leq |r| \leq a\dfrac{1+\alpha}{2} \\ -1 & if\ a\dfrac{1+\alpha}{2} \leq |r| \leq a \end{cases} \tag{1}$$

Similarly, the next step is to scale the function in order to limit its extent between $n_1$ and $n_2$ (maximum refractive index at the core cladding interface, and minimum refractive index at the core center, respectively). We shift and scale the function in the form of $A + B \times tanh[\frac{\pi}{\alpha}((r-\frac{a}{2})/\frac{a}{2})]/tanh(\pi)$, where $A = (n_1+n_2)/2$, and $B = \Delta n/2$. The obtained HTAN distribution $n(r)$ is as follows:

$$n(r) = \begin{cases} n_2 \\ \quad if\ 0 \leq |r| \leq a\dfrac{1-\alpha}{2}\ (core) \\ \dfrac{n_1+n_2}{2} + \dfrac{\Delta n}{2\ tanh(\pi)} tanh(\pi \dfrac{(r-a_1)}{a_1\alpha})) \\ \quad if\ a\dfrac{1-\alpha}{2} \leq |r| \leq a\dfrac{1+\alpha}{2}\ (core) \\ n_1 \\ \quad if\ a\dfrac{1+\alpha}{2} \leq |r| \leq a\ (core) \\ n_3 \\ \quad if\ \ |r| \geq a\ (cladding) \end{cases} \tag{2}$$

where $n_1$, $n_2$, $n_3$ are the three levels of refractive index as illustrated in Fig. 2, $a$ and $\alpha$ are the core radius and the shape parameter, respectively, and $r$ denotes the distance from core center. $\Delta n = n_1 - n_2$ corresponds to the extent of hyperbolic tangent function, and $a_1 = a/2$. At core subbounds: $a(1-\alpha)/2$ and $a(1+\alpha)/2$, $n(r) = n_2$ and $n(r) = n_1$, respectively. The parameter $\alpha$, where $0 \leq \alpha \leq 1$, controls the shape behavior of HTAN function and will also be referred to as smoothness parameter. Considering the special case of $\alpha = 0$, HTAN corresponds to the known step index inner & outer ring core fiber. From Figure 2, one can see that the proposed HTAN-fiber has quite similar profile complexity (i.e. inner graded & outer Sharpe variation) like IPGI

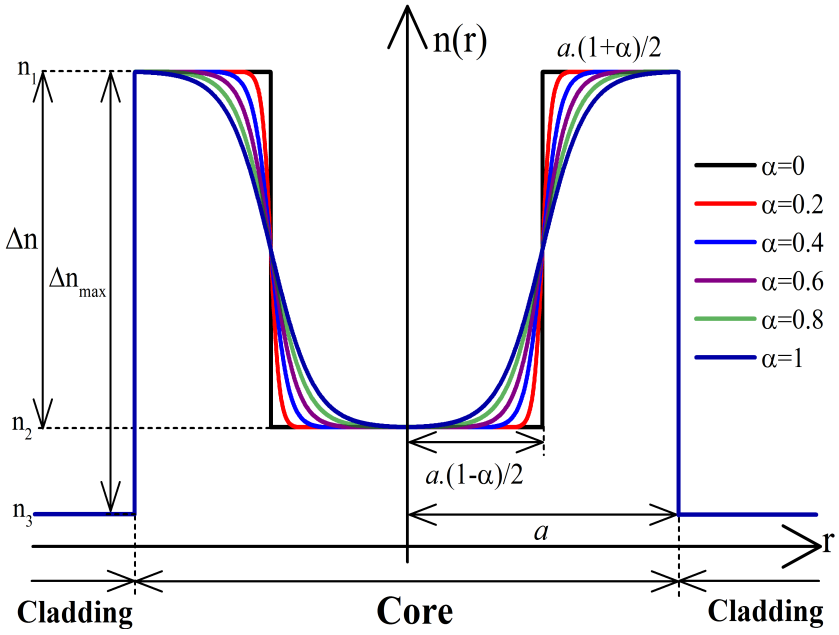


**FIGURE 2.** Refractive index profile of HTAN fiber for different values of profile shape $\alpha$.

fiber [21] but simpler than VF [9] and GIRC fiber [18] where both fibers observe an interior and outer graded refractive index evolution''.

## III. FIBER KEY PARAMETERS AND INTER-CHANNELS SEPARATION

We theoretically investigate and numerically validate the modal separation between supported vector modes in the proposed HTAN fiber. In this section, we investigate the fiber parameters that directly influence the intermodal separation. However, this helps to optimize the fiber-improved separation between propagating modes. In [21], [27] the authors proposed/introduced a theoretical analysis of intermodal separation inside optical fiber by applying a first order perturbation. We exploited their analysis and applied it for our proposed profile index. Ung and co-workers stated that wide effective index separation between vector modes require: (1) Large refractive index gradient expressed as $\vec{\nabla}(ln(n^2))$ (e.g. Sharp core-cladding boundary together with large refractive index separation (contrast, jump)), (2) high transverse field amplitudes ($\vec{e}$), and (3) large field variation $\vec{\nabla}.\vec{e}$.

Intuitively, one of the most attractive criteria in hyperbolic tangent function, used as an activation function in neural network, is its strong gradient centered around the inflection point (switch point). In Appendix I, we provide the theoretical approach used for identifying the fiber parameters that control the effective index separation behavior. In Appendix I, by applying the expression of gradient (A.12) on HTAN refractive index distribution (core region), and evaluating it at the sub-bound $a(1+\alpha)/2$, we find the following proportionality relation:

$$\Delta n_{\text{eff}} \propto \frac{\Delta n}{\alpha a n_1} \tag{3}$$

Theoretically, for HTAN profile, the effective index separation is proportional to the relative refractive index difference inside the core $\Delta n/n_1$ while it is inversely proportional to the shape parameter $\alpha$ and to the core radius $a$. Hence, any variation in either of these fiber parameters changes automatically the intermodal separation. The mode field and the mode field gradient have been numerically computed using FEM (A.8). Fig. 3 (a and c) depicts the normalized transverse electric fields $TE_{0,1}$ and $HE_{2,1}$ together with simulated refractive index profile of HTAN profile with $\alpha = 1$ and $\alpha = 0.5$, respectively, while Fig. 3(b and d) shows its corresponding gradients in cylindrical coordinates. From Fig. 3(b and d), one can see that both maxima of gradients superpose at the same point (core-cladding boundary ($r = a$). Moreover, quantities have the same sign (negative here). This means that high effective index separation between vector modes is accomplishable in the proposed HTAN fiber.

In order to both prove (validate) the obtained relation (3) and optimize the fiber parameters (improve $\Delta n_{\text{eff}}$), we investigate the intermodal separation between $TE_{0,1}$, $HE_{2,1}$, and $TM_{0,1}$ that forms the mode group $G_2$. The selection of $G_2$ (known as $LP_{1,1}$) comes from the fact that $TE_{0,1}$ and $TM_{0,1}$ are parasitic modes that do not provide an OAM mode and induce crosstalk to the other OAM modes $OAM_{\pm 1,1}$ if they are not enough spaced. In addition, as revealed from [21], the higher order modes ($HE_{1,m}/EH_{1,m}$) with the same radial number ($m = 1$) share the same intermodal separation behavior. We aim to validate the theoretical investigation highlighted above, and optimize $\alpha$, $\Delta n_{\max}$, $\Delta n$ and $a$ for the fiber design in order to achieve wide effective index separation among vector modes belonging to $G_2$.

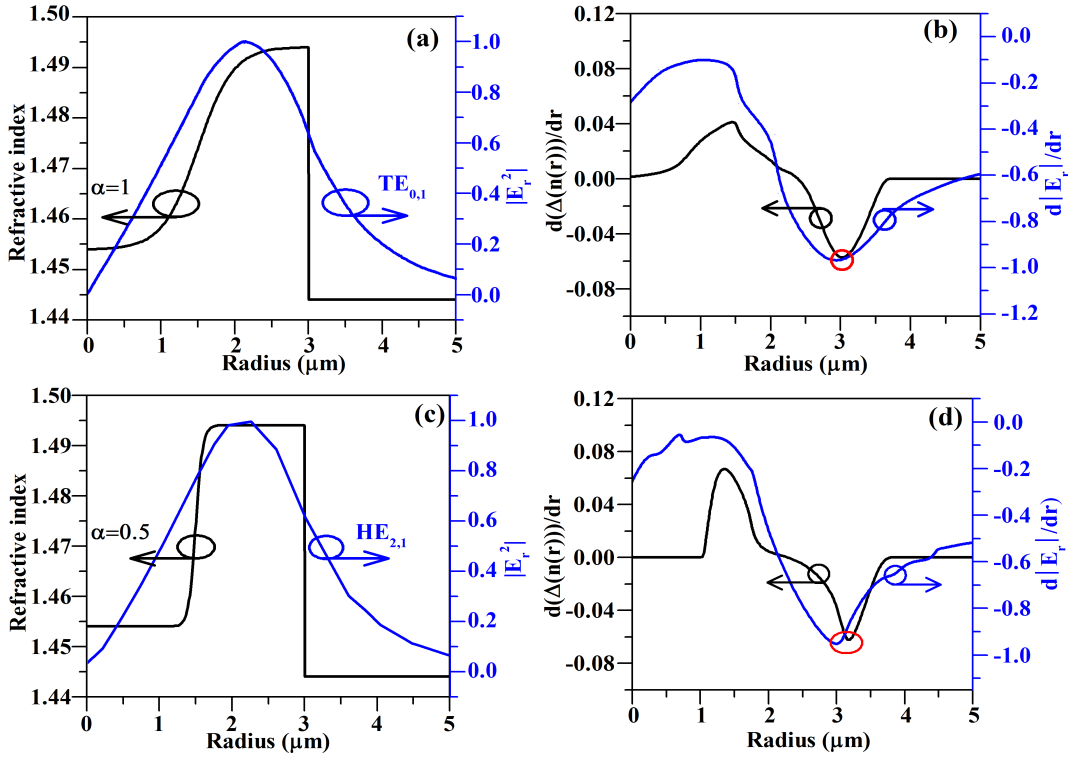


**FIGURE 3.** (a) Normalized E-field intensity of the $TE_{0,1}$ and HTAN refractive index profile for $\alpha = 1$, (b) The gradient of E-field amplitude (normalized) of $TE_{0,1}$ mode and those of simulated refractive index profile $\alpha = 1$. (c) Normalized E-field intensity of the $HE_{2,1}$ and HTAN refractive index profile for $\alpha = 0.5$, (d) The gradient of E-field amplitude (normalized) of $HE_{2,1}$ mode and those of simulated refractive index profile $\alpha = 0.5$. Other fiber parameters are $a = 3\mu m$, $\alpha = 1$, $\Delta n_{max} = 0.05$, $\Delta n = 0.04$, and $n_3 = 1.444$.

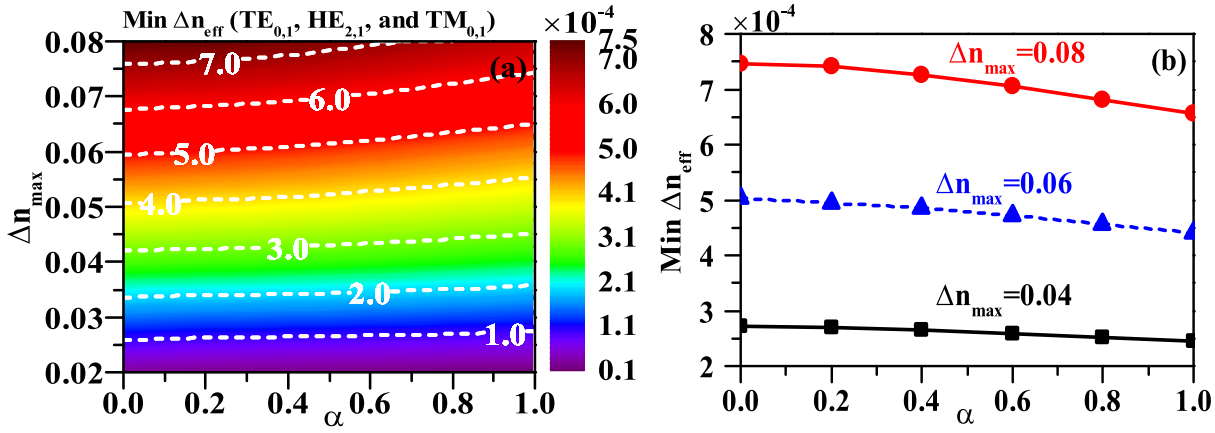


**FIGURE 4.** (a) Minimum effective index separation between ($TE_{0,1}$, $HE_{2,1}$, and $TM_{0,1}$) as a function of shape factor $\alpha$ and $\Delta n_{max}$. (b) Isolines along selected contrast values: $\Delta n_{max} = [0.04, 0.06, 0.08]$.

### *A. INTER-CHANNELS SEPARATION VERSUS THE SHAPE $\alpha$ AND REFRACTIVE INDEX CONTRASTS*

We investigate the minimum intermodal separation $\Delta n_{\text{eff}}$ among ($TE_{0,1}$, $HE_{2,1}$, and $TM_{0,1}$). Fig. 4 (a) depicts the minimum $\Delta n_{\text{eff}}$ inside $G_2$ versus the shape parameter ($\alpha$) and the maximum contrast between core and cladding indexes ($\Delta n_{\text{max}}$). In addition, Fig. 4(b) shows the minimum $\Delta n_{\text{eff}}$ versus $\alpha$ for selected values of $\Delta n_{\text{max}}$. It is clear that for a given value of $\alpha$, $\Delta n_{\text{eff}}$ increases with the increase of $\Delta n_{\text{max}}$. This confirms that a high contrast refractive index between fiber core and cladding favors large $\Delta n_{\text{eff}}$, enabling low intermodal crosstalk. Furthermore, from Fig. 4(a) a very large $\Delta n_{\text{eff}}$ of around $7.5 \times 10^{-4}$ is achievable with ultra large $\Delta n_{\text{max}} = 0.08$. This value is experimentally achievable with modified chemical vapor deposition (MCVD) process with Germania doped silica [28]. On the other hand, Fig. 4(b) reveals that for selected values of $\Delta n_{\text{max}}$, $\Delta n_{\text{eff}}$ inside $G_2$ slowly decreases with $\alpha$. The impact of actual refractive

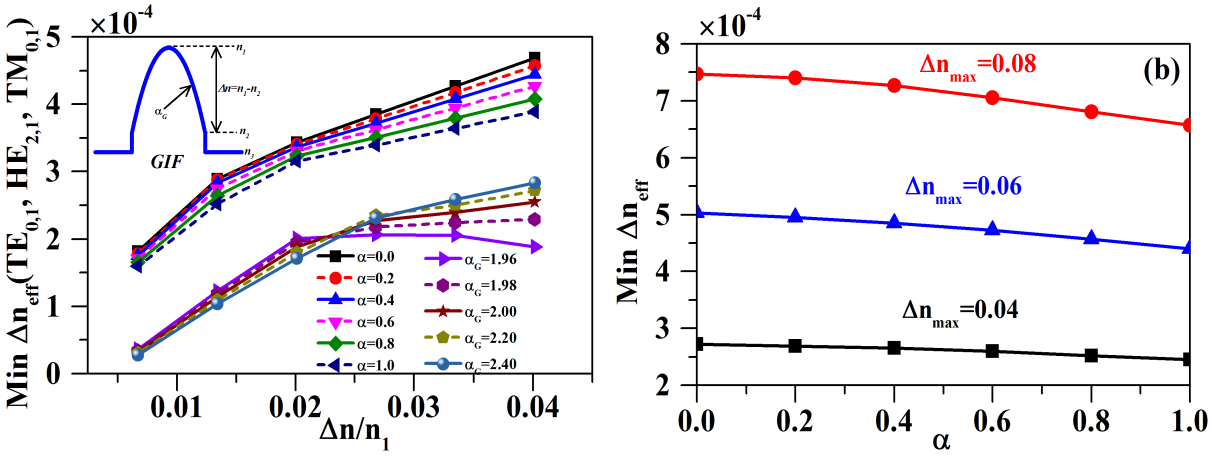


**FIGURE 5.** Minimum effective index separation between ($TE_{0,1}$, $HE_{2,1}$, and $TM_{0,1}$) as a function of: (a) the relative difference $\Delta = \Delta n/n_1$ and for various smoothness parameter $\alpha$, collocated with those calculated in GIF (for different $\alpha_G$) (b) the smoothness parameter and for various values $\Delta$n, $a = 3\mu$m, $\lambda = 1.55\mu$m, and $\Delta n_{max} = 0.05$.

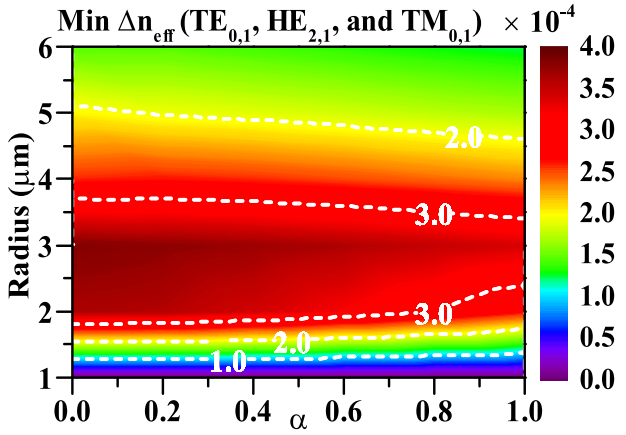


**FIGURE 6.** Minimum effective index separation between ($TE_{0,1}$, $HE_{2,1}$, and $TM_{0,1}$) as a function of smoothness parameter $\alpha$ and the core radius $a$, $n_3 = 1.444$, $\Delta n_{max} = 0.05$, $n_2 = 1.454$ and $\lambda = 1.55$ $\mu$m.

index difference ($\Delta n = n_1 - n_2$) on $\Delta n_{\text{eff}}$ is investigated. In Fig. 5(a), the minimum $\Delta n_{\text{eff}}$ inside $G_2$ is depicted versus the relative refractive index difference inside the core ($\Delta n/n_1$) for a given shape parameter $\alpha$. In order to evaluate the effects of $\alpha$ on $\Delta n_{\text{eff}}$, we add the $\Delta n_{\text{eff}}$ in standard graded index fiber (GIF) simulated with the same parameters as in HTAN fiber for different values of shape parameter ($\alpha_G$). In Fig. 5(b), we depict minimum $\Delta n_{\text{eff}}$ versus $\alpha$ for given values of $\Delta n$. Figure 5(a) confirms that $\Delta n_{\text{eff}}$ increases with $\Delta n$ as predicted by expression (3). Furthermore, HTAN improves the intermodal separation compared to the standard GIF.

### B. INTER-CHANNELS SEPARATION VERSUS CORE RADIUS

Fig. 6 highlights the minimum $\Delta n_{\text{eff}}$ inside $G_2$ versus $a$ and $\alpha$. We observe that small core (at the vicinity of $3\mu m$) enhances the intermodal separation ($a \leq 3.5\mu m$, $\Delta n_{\text{eff}} \geq 3.5 \times 10^{-4}$). In order to investigate and validate the theoretical studies above more, we calculate $\Delta n_{\text{eff}}$ : $TE_{0,1} - HE_{2,1}$ and $HE_{2,1} - TM_{0,1}$ versus the core radius for selected partical values of maximum contrast $\Delta n_{\max}$: [0.04, 0.05, and 0.06], for selected values of the difference $\Delta n$:[0.03, 0.04, and 0.05] and for different values of shape parameter $\alpha$ (Fig 7 (a-d)).

One can see that the modal separation increases with core radius until it reaches its maximum (peak) at an optimal core radius $a_{opt}$. Interestingly, when $r \leq a_{opt}$, we find $\Delta n_{\text{eff}}$ ($TE_{0,1}$, $HE_{2,1}$) $\geq \Delta n_{\text{eff}}$ ($HE_{2,1}$, $TM_{0,1}$). On the other hand, when $r \geq a_{\text{opt}}$, we find $\Delta n_{\text{eff}}$ ($HE_{2,1}$, $TM_{0,1}$) $\geq \Delta n_{\text{eff}}$ ($TE_{0,1}$, $HE_{2,1}$). This indicates that the vector modes ($TE_{0,1}$, $HE_{2,1}$, and $TM_{0,1}$) formed $LP_{1,1}$ are spaced regularly at $a_{opt}$. Hence, the located $a_{opt}$ is useful for directing the design ($\Delta n_{\max}$ & $\Delta n$) of HTAN fiber towards the improvement of intermodal separation.

## IV. OAM MODES ANALYSIS

In this section, we select the fiber parameters that enhance the separation among first radial OAM modes. We then generate the OAM modes and assess its purity and the induced intrinsic crosstalk at fixed wavelength $\lambda = 1.55$ $\mu m$. Subsequently, we expand the wavelength band to cover the entire C (ITU-T) band ranging from 1525 $nm$ to 1625 $nm$, where we investigate the impact of the shape parameter "$\alpha$" on various performance metrics including chromatic dispersion, and differential group delay.

### A. SELECTED PARAMETERS

Considering all the modes, Fig 8 highlights the $\Delta n_{\text{eff}}$ between successive modes versus "$a$" for selected values of $\Delta n_{\max}$, $\Delta n$ and for different values of "$\alpha$". The vertical lines correspond to the supported eigenmodes number boundary. We ignored the part when $\Delta n_{\text{eff}} < 10^{-4}$. Each sub-figure (map) could be considered as ID card for fiber (for each $\alpha$) since it provides number & order of modes, separation among them, and the optimum fiber parameter values (cutoff radii, $\Delta n_{\max}$, and $\Delta n$). From those figures, it is confirmed that $\Delta n_{\text{eff}}$ between first radial modes ($m = 1$) decreases as "$a$" increases while it increases for higher radial modes, (e.g. $HE_{1,2}$ lines without symbols).

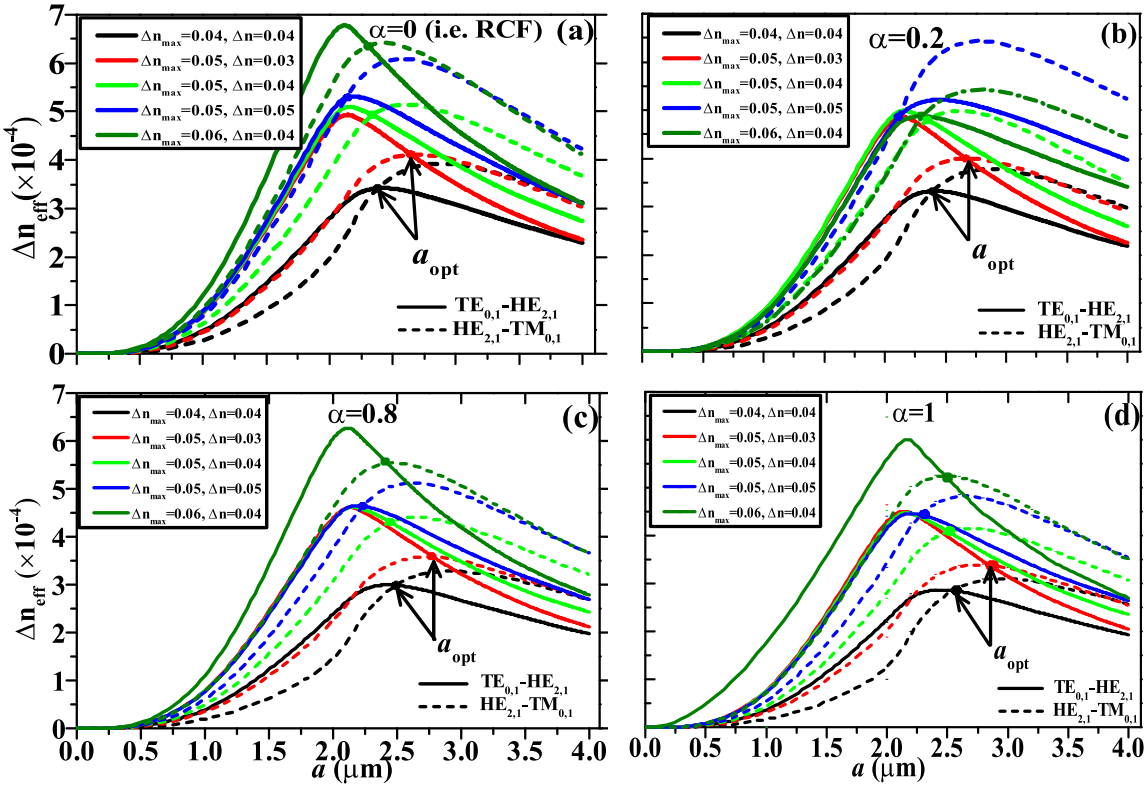


**FIGURE 7.** Effective index separation between ($TE_{0,1}$, $HE_{2,1}$, and $TM_{0,1}$) as a function of core radius and for different values of maximum contrast $\Delta n_{max}$, refractive index difference $\Delta n$, and shape parameter $\alpha$.(a) $\alpha = 0$, (b) $\alpha = 0.2$, (d) $\alpha = 0.8$, and (d) $\alpha = 1$.

Interestingly, $\Delta n$ intervenes in the order of excited mode: when $\Delta n$ decreases; it tends to delay the excitation of higher radial order modes (e.g. $HE_{1,2}$, comparison between $\Delta n = 0.04$ and $\Delta n = 0.05$) while it decreases $\Delta n_{\text{eff}}$ among modes. Thus, a trade-off-design should be considered between mode number, $\Delta n_{\text{eff}}$ between modes as well as the mode order (i.e. $m$).

Since higher radial orders OAM modes cause trouble in multiplexing and demultiplexing operations due to the intensity and phase variety distribution (complex modal distribution), we limited our study to the first radial OAM modes that fulfil the criteria $\Delta n_{\text{eff}} > 10^{-4}$. Hence, there are 10 possible eigenmodes. Moreover, the HTAN-FMF will perform comparably to several other OAM-fibers by supporting higher order OAM modes packaging into mode groups (MG) where the inter-MG separation should be maintained with more tradeoffs.

Based on the theoretical and numerical analysis above, we select the fiber parameters that both enhance $\Delta n_{eff}$ among large vector modes number and favor the formation of first order-OAM modes as follows: $a = 3\mu m$, $n_3 = 1.444$, $\Delta n_{max} = 0.05$ and $\Delta n = 0.04$. With such parameters, the proposed HTAN-FMF supports 10 eigenmodes, divided into 3 groups: $G_1(HE_{1,1})$, $G_2(TE_{0,1}, HE_{2,1}, TM_{0,1})$ and $G_3(EH_{1,1}, HE_{3,1})$.

At last, we denote OAM modes as $OAM^{\pm}_{\pm l,m}$ where $\pm$ superscript describes the spin angular momentum SAM (circular polarization). $l$ and $m$ subscript denote the azimuthal and radial indices, respectively, and $m$ describes the number of nulls radially (rings) in the intensity profile of the OAM mode. Fig. 9 recapitalizes the guided vector modes supported in HTAN fiber with the parameters cited under the graph. In addition, we depict the corresponding OAM modes generated by combining the even and odd modes of $HE_{l,m}$ or $EH_{l,m}$ modes with $\pm$ ($\pi$/2) phase shift calculated using finite element method (FEM) [29]. The combination between $TE_{0,1}$ and $TM_{0,1}$ do not provide OAM states due to the large separation between its propagation constants.

All the modes are sufficiently spaced (above $10^{-4}$) enabling low crosstalk between different channels. The obtained $\Delta n_{eff}$ at $\lambda = 1.55$ $\mu$m are $6.47 \times 10^{-3}$ between ($OAM^{\pm}_{\pm 0,1}$, $TE_{0,1}$), $3.40 \times 10^{-4}$ between ($TE_{01}$, $OAM^{\pm}_{\pm 1,1}$), $4.07 \times 10^{-4}$ between ($OAM^{\pm}_{\pm 1,1}$, $TM_{01}$), $1.26 \times 10^{-2}$ between ($TM_{01}$, $OAM^{\mp}_{\pm 2,1}$), and $1.66 \times 10^{-4}$ between ($OAM^{\mp}_{\pm 2,1}$, $OAM^{\pm}_{\pm 2,1}$). To the best of our knowledge, the proposed fiber achieves the largest reported effective indices separation between ($TE_{0,1}$, $OAM^{\pm}_{\pm 1,1}$ and $TM_{0,1}$) in comparison to known OAM-FMFs (see Table 1). This enables low inter-channel crosstalk making the proposed fiber suitable for transporting OAM modes. Morover, inspired from the IPGI experiment results (3.36 Tbits/s using 4 OAM and 15 WDM [22]), we believe that using the same experiment process, an agreggate capacity of more than 7 Tbit/s can be achieved using HTAN-FMF incorporating 8 OAM modes carrying data.

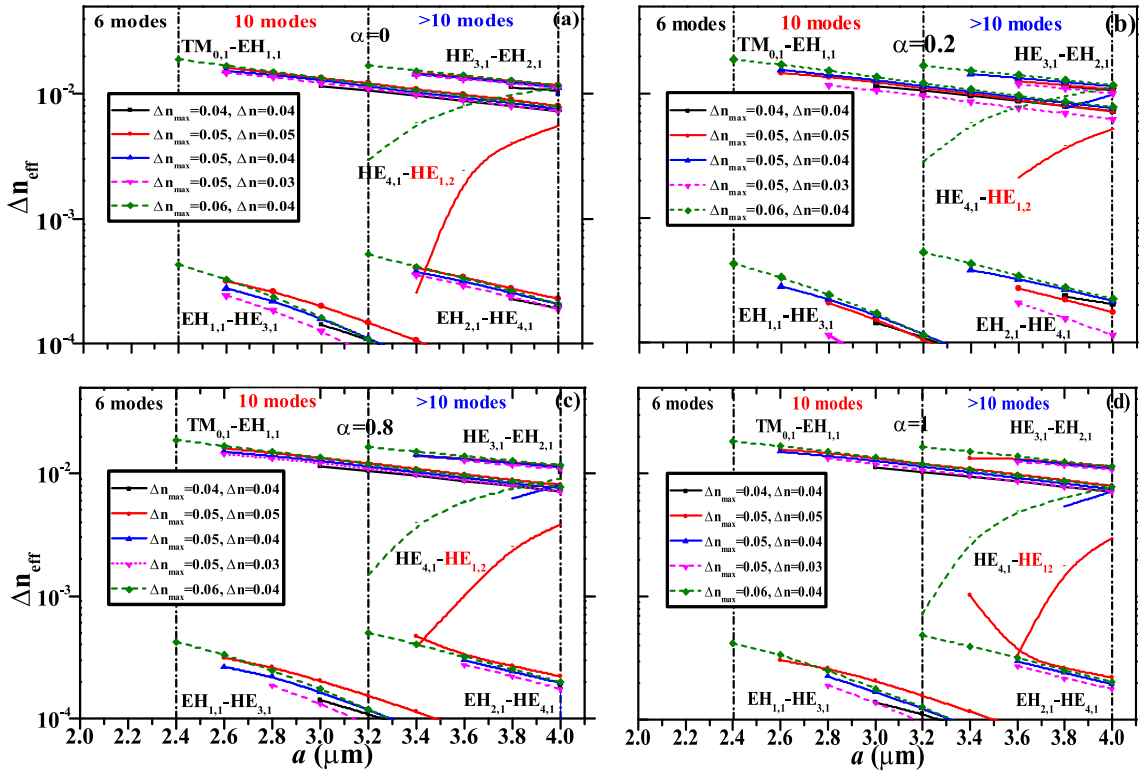


**FIGURE 8.** Effective index separation between successive modes as a function of core radius and for different values of maximum contrast $\Delta n_{max}$, refractive index difference $\Delta n$, and for different values of shape parameter $\alpha$. (a) $\alpha = 0$, (b) $\alpha = 0.2$, (d) $\alpha = 0.8$, and (d) $\alpha = 1$.

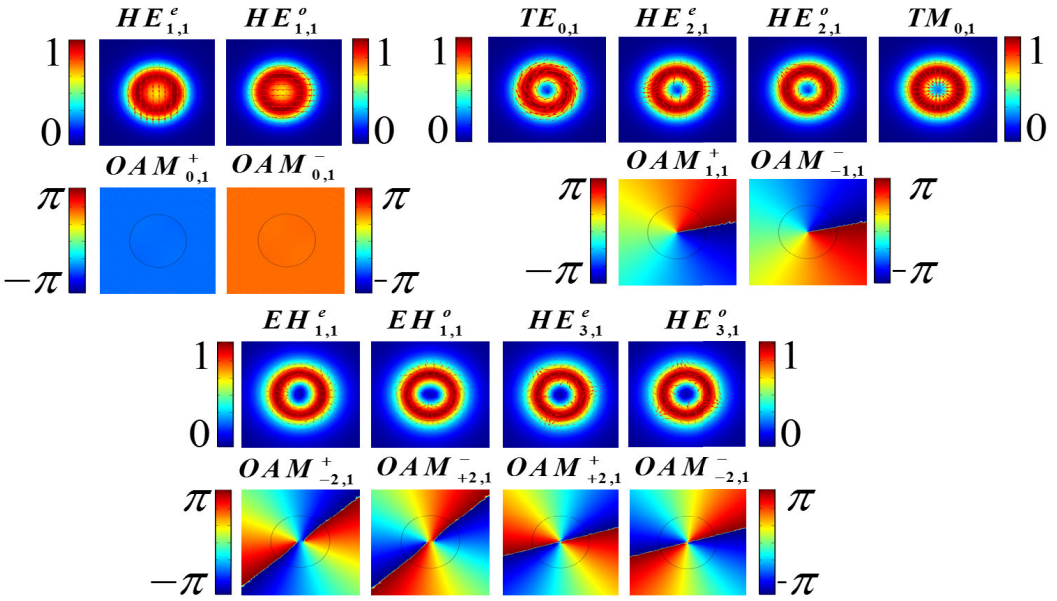


**FIGURE 9.** Normalized electric field, normalized amplitude (Rainbow scale) and direction of transverse electric field (Red arrows) of all guided vector modes (even and odd) in the HTAN profile regrouped into three groups. The graph shows a part of spatial phase distributions of the dominant component electric field of the generated OAM modes. The fiber parameters are kept as $a = 3$ $\mu$m, $n_3 = 1.444$, $n_2 = 1.454$, $\Delta n_{max} = 0.05$, and $\lambda = 1.55$ $\mu$m.

### B. OAM MODE QUALITY

In order to qualitatively assess (evaluate) the obtained OAM modes in the proposed HTAN-FMF and evaluate the distribution impact, we investigate the OAM purity in the designed fiber. Interestingly, it has been demonstrated in [24] that the refractive index profile structure intervenes in enhancing the OAM purity enabling low induced intrinsic crosstalk. The attention of authors was concentrated on the evolution of

**TABLE 1. The effective index separation in HTAN-FMF compared to those in recently reported OAM-FMF.**

| Specialty OAM-fiber | Mode number | Min [$\Delta n_{eff}$] @ $\lambda$=1.55$\mu m$ |
|---|---|---|
| HTAN-FMF ($\alpha = 1$) | 8 $l = [0, \pm1, \pm2]$ | $3.4\times10^{-4}$ $(TE_{0,1}/OAM^{\pm}_{\pm1,1}/TM_{0,1})$ $1.66\times10^{-4}$ $(OAM^{\pm}_{\pm2,1})$ |
| HTAN-FMF ($\alpha = 0$) | 8 $l = [0, \pm1, \pm2]$ | $3.9\times10^{-4}$ $(TE_{0,1}/OAM^{\pm}_{\pm1,1}/TM_{0,1})$ $1.61\times10^{-4}$ $(OAM^{\pm}_{\pm2,1})$ |
| Vortex fiber [9] | 2 $l = [\pm1]$ | $1.8\times10^{-4}$ $(TE_{0,1}/OAM^{\pm}_{\pm1,1}/TM_{0,1})$ |
| IPGI [21] | 8 $l = [0, \pm1, \pm2]$ | $2.1\times10^{-4}$ $(TE_{0,1}/OAM^{\pm}_{\pm1,1}/TM_{0,1})$ $1.6\times10^{-4}$ $(OAM^{\pm}_{\pm2,1})$ |
| ACF [12] | 36 $l = [0, \pm1, \pm2, ..., \pm9]$ | $1.1\times10^{-4}$ $(TE_{0,1}/OAM^{\pm}_{0,1})$ |
| RCF [15] | 8 $l = [0, \pm1, \pm2]$ | $1.1757\times10^{-4}$ $(TE_{0,1}/OAM^{\pm}_{\pm1,1}/TM_{0,1})$ $0.8065\times10^{-4}$ $(OAM^{\pm}_{\pm2,1})$ |
| IRCF [20] | 8 $l = [0, \pm1, \pm2]$ | $3.04\times10^{-4}$ $(TE_{0,1}/OAM^{\pm}_{\pm1,1}/TM_{0,1})$ $1.78\times10^{-4}$ $(OAM^{\pm}_{\pm2,1})$ |

refractive index from the core center till the cladding region (graded versus step). They demonstrated theoretically that outer graded index structure enhances OAM purity in contrast to step index structures (straight evolution). They draw our attention to the effects of the shape factor $\alpha$ (in HTAN-FMF) on the synthetized OAM's purity.

Investigating the purity versus the parameter $\alpha$ seems to be justifiable since the only fiber parameter that controls the shape profile in HTAN fiber is the parameter $\alpha$. In addition, this choice helps to evaluate the impact of the only inner smooth behavior of hyperbolic tangent function on the fiber performance, which is one of the main purposes of this research. Considering all the OAM states ($OAM^{\pm}_{\pm l,m}$), we calculate the power weight of major and minor OAM light beams through processing the integral of right part constituting the transverse field of OAM modes versus the shape factor $\alpha$ expressed as [30]:

$$\begin{aligned} V^{\pm} = & \frac{kn_{eff}A}{[k^2(n_{HTAN}(r))^2 - (kn_{eff})^2]} \\ & \times (\pm\overrightarrow{y} - i\overrightarrow{x})(1+s)P(r)e^{\pm i(l+1)\Theta} \\ & \pm(\mp\overrightarrow{y} - i\overrightarrow{x})(1-s)Q(r)e^{\pm i(l-1)\Theta} \end{aligned} \quad (4)$$

where $k$, $n_{eff}$ and $n_{HTAN}$ are the wave number in vacuum, mode effective index, and the refractive index of HTAN profile at given $\alpha$, respectively. $\overrightarrow{x}$ and $\overrightarrow{y}$ are two orthogonal unit vectors of cartesian coordinates. $s$, $P(r)$ and $Q(r)$ are given as follows: $s \equiv \frac{\omega\mu_0 C}{kA}$, $P(r) \equiv \frac{1}{2}[\frac{\partial F_{lz}(r)}{\partial r} + \frac{1}{r}F_{lz}(r)]$ and $Q(r) \equiv \frac{1}{2}[\frac{\partial F_{lz}(r)}{\partial r} - \frac{1}{r}F_{lz}(r)]$. $A$ and $C$ are undetermined coefficients and $F_{lz}(r)$ is the radial dependance of the field profile. The OAM purity are depicted in Fig. 10 (a). In addition, we calculate the corresponding induced intrinsic crosstalk. The purity and the intrinsic crosstalk of OAM light beam are respectively calculated as [30]:

$$Purity = \frac{OAM_{major}}{OAM_{major} + OAM_{minor}} \quad (5)$$

and

$$\begin{aligned} IntrinsicCrosstalk &= \frac{OAM_{minor}}{OAM_{major} + OAM_{minor}} \\ &= 1 - Purity \end{aligned} \quad (6)$$

where OAM major/minor is the power weight of the major/minor OAM modes. It is clear that the OAM purity increases with the increase of $\alpha$. Hence, as the profile interiorly smooths, the OAM purity improves. This is confirmed by the increase of OAM purity of $OAM^{\pm}_{0,1}$, $OAM^{\pm}_{\pm1,1}$, $OAM^{\mp}_{\pm2,1}$ and $OAM^{\pm}_{\pm2,1}$ versus $\alpha$. The minimum OAM purity is found at $\alpha = 0$ which corresponds to step ring core structure. In step ring core structure, the refractive index presents two discontinuity areas with large refractive index contrast. The first is located at $r = a/2$ (inner core) when the refractive index "jumps" from $n_2$ to $n_1$, while the second is located at $r = a$ (outer core), the area at which the refractive index 'falls' from $n_1$ to $n_3$. Except $OAM_{0,1}$, all the OAMs' purity are below 99.9%. Recalling here that an OAM purity of 99.9% is equivalent to an intrinsic crosstalk of $-30$dB. This key value is a theoretical limit of the practical crosstalk of the OAM optical fiber communication networks [30]. The worst purity is for $OAM^{\mp}_{\pm2,1}$ valuing 69.907% (intrinsic crosstalk = $-5{,}215$dB). Moreover, given the fact that $\alpha = 1$ corresponds to the slow changes of refractive index, it presents the highest OAM purity compared to other $\alpha$ values. The OAM purity of $OAM^{\pm}_{0,1}$, $OAM^{\pm}_{\pm1,1}$,$OAM^{\mp}_{\pm2,1}$ and $OAM^{\pm}_{\pm2,1}$ (at $\alpha = 1$) are 99.960%, 99.971%, 99.814% and 99.965%, which correspond to intrinsic crosstalk of $-33.97$ $dB$, $-35.37$ $dB$, $-27.30$ $dB$ and $-34.55$ $dB$, respectively. The lower value of OAM purity of $OAM^{\mp}_{\pm2,1}$ can be attributed to the high contrast between core and cladding refractive indexes ($\Delta n_{\max}$) and/or the step index interface at the vicinity between the core and the cladding ($r = a$), hence presenting discontinuity area that enhances the anti-aligned spin orbit coupling that deteriorates the synthetized OAM purity. Even though, this value is larger than those in vortex fiber [9] (99.8%), and comparable to those in designed known graded index FMF in [30] and in IRCF [20].

## V. TRANSMISSION PERFORMANCE METRICS ACROSS TELECOMMUNICATION BANDS

The wide separation at fixed wavelength ($\lambda = 1.55\mu$m) has been analyzed and discussed in previous sections. Here, we extend the wavelength to cover the entire C&L (ITU-T) bands, ranging from 1525 nm to 1565 nm. We assessed the OAM modes separation over C&L, the chromatic dispersion (CD) and differential group delay (DGD) both over C band.

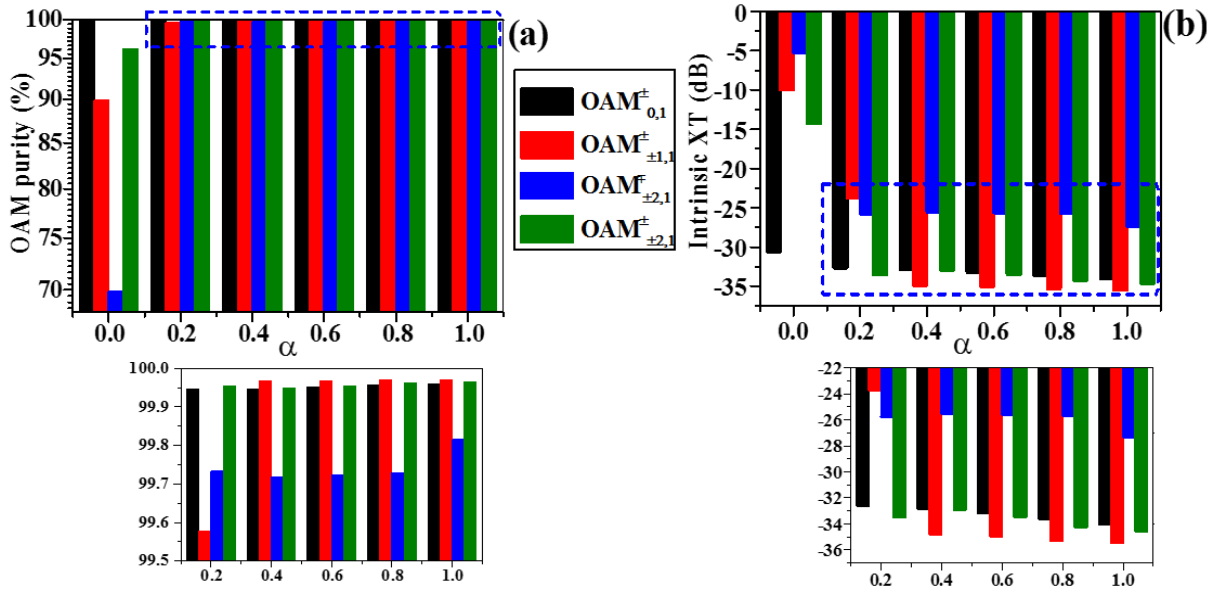


**FIGURE 10.** (a) OAM purity (%), (b) intrinsic crosstalk (dB) in HTAN fiber; as a function of $\alpha$ for OAM modes, $a = 3\mu$m, $n_3 = 1.444$, $n_2 = 1.454$, $\Delta n_{max} = 0.05$ and $\lambda = 1.55\mu$m.

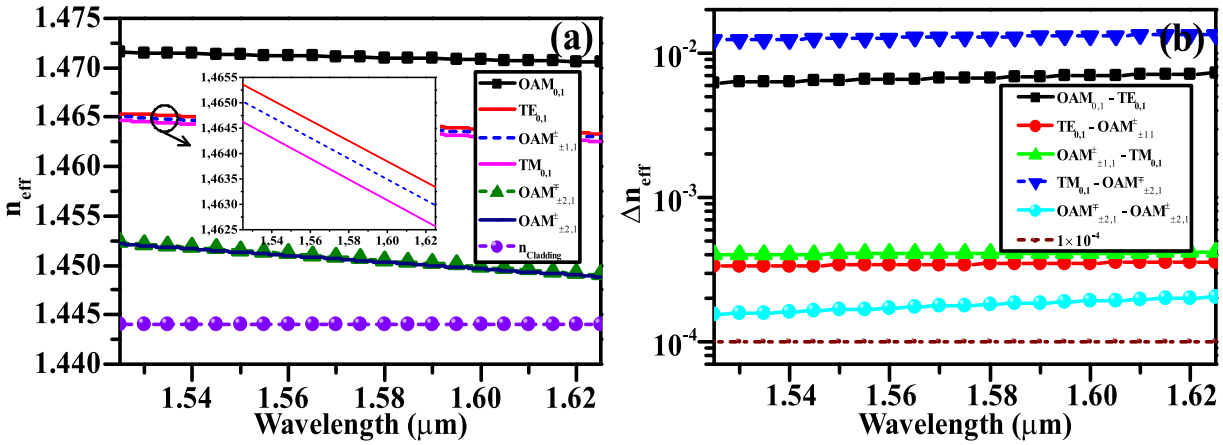


**FIGURE 11.** (a) Effective indices of modes (neglecting the polarization degenerate modes) of the designed HTAN ($\alpha = 1$), (b) the corresponding effective indices separation between successive modes across the C+L band.

### A. INTER-CHANNELS CROSSTALK ACROSS C+L BAND

We investigate the effective indices separation between all supported modes along the selected bands. Using FEM, Fig. 11 (a) depicts the mode effective indices versus the wavelength. The proposed HTAN-FMF supports eight OAM modes in the entire C+L band. These OAM modes are divided into 3 groups: $G_1$ ($OAM^{\pm}_{0,1}$), $G_2$ ($TE_{01}$, $OAM^{\pm}_{\pm1,1}$, $TM_{01}$) and $G_3$ ($OAM^{\mp}_{\pm2,1}$,$OAM^{\pm}_{\pm2,1}$). On the other hand, we investigate the effective indices differences between successive modes (inter and intra-group separation) across the wavelength. The results are shown in Fig. 11 (b). The $\Delta n_{\text{eff}}$ between adjacent modes slowly increases with wavelength. All the modes are sufficiently spaced (above $10^{-4}$) enabling low crosstalk between different channels.

### B. CHROMATIC DISPERSION ACROSS C BAND

The chromatic dispersion (CD) of supported modes is evaluated through the following expression [20]:

$$CD = \frac{-\lambda}{c}\frac{\partial^2 n_{eff}}{\partial \lambda^2} \tag{7}$$

where $\lambda$ and $c$ are the wavelength and the light velocity both in vacuum, respectively. $n_{eff}$ is the mode effective index. the results are depicted in Fig. 12 for different values of $\alpha$= [0, 0.2, 0.8, and 1]. One can clearly see that the chromatic dispersion curves are flat, negative or slowly decreases with wavelength for $G_1$ ($OAM^{\pm}_{0,1}$) and $G_2$ ($TE_{0,1}$/ $OAM^{\pm}_{\pm1,1}$/$TM_{01}$), while it decreases significantly versus wavelength for $G_3$ ($OAM^{\mp}_{\pm2,1}$,$OAM^{\pm}_{\pm2,1}$). The effective indices of $OAM^{\mp}_{\pm2,1}$ and $OAM^{\pm}_{\pm2,1}$ are close to the cutoff index (refractive index of

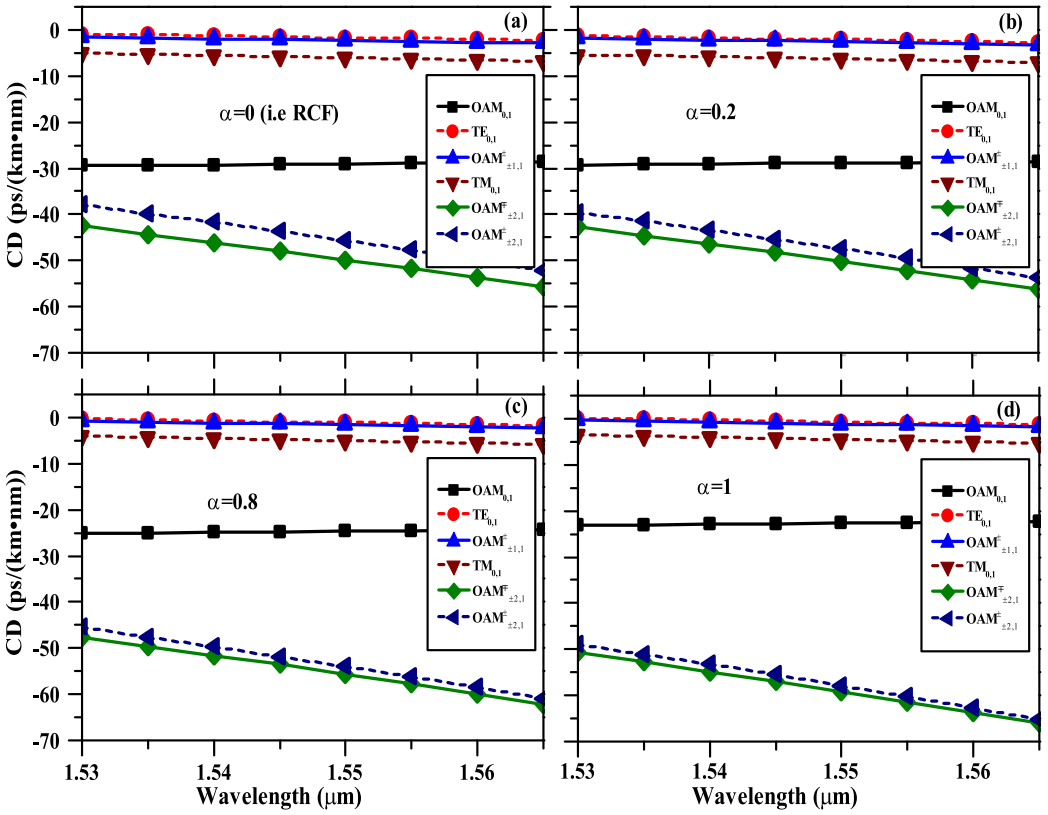


**FIGURE 12.** The chromatic dispersion of modes (neglecting polarization degenerate modes) of the designed HTAN across the C band for different values of $\alpha$: (a) $\alpha = 0$, (b) $\alpha = 0.2$, (c) $\alpha = 0.8$, and (d) $\alpha = 1$.

cladding), hence placing the dispersion in high value range around −60 (ps/(km.nm)) compared to the chromatic dispersion of $G_1$ and $G_2$.

Considering the effect of $\alpha$ on mode chromatic dispersion, Fig. 12 provides that the chromatic dispersion of $G_1$ and $G_2$ slowly decreases with $\alpha$ (the chromatic dispersion get close to zero as $\alpha$ increases). On the other hand, the chromatic dispersion of $G_3$ increases with $\alpha$. This behavior may be explained by the impact of the shape parameter $\alpha$ on the profile structure. When the shape parameter $\alpha$ increases, the effective difference between the radii of the inner and outer cores reduce, and the higher mode effective indices approach the cutoff index (i.e. the cladding ($n_3$)).

Considering the case when $\alpha = 1$, over the whole C band, the $G_1$ and $G_2$ dispersions are less than 30 (ps/(km.nm)) while larger for the third group (about 60 (ps/(km.nm))). These dispersion values are close to those obtained for air core fiber reported in [31] (> 62 (ps/(km.nm))) or in ring core fiber [31] (> 39.7 (ps/(km.nm)). The dispersion properties of designed fiber are promising since they are lower than those in the reported IPGI-FMF (around −100 (ps/(km.nm))) for $G_3$) [21] and air core fiber [14]. Hence, HTAN-FMF is quite promising for long distance fiber communication using OAM modes carrying data.

### C. DIFFERENTIAL GROUP DELAY ACROSS C BAND

We investigate the differential group delay (DGD) of OAM modes.In principle, the DGD of given mode ($OAM^{\pm}_{\pm l,m}$) is calculated considering the first mode ($OAM^{\pm}_{0,1}$) using [20]:

$$DGD = \tau_{(OAM^{\pm}_{0,1})} - \tau_{(OAM^{\pm}_{\pm l,m})} \tag{8}$$

where $\tau$ is the mode delay. the results are calculated for different values of $\alpha$= [0, 0.2, 0.8 and 1] (Fig.13).

The DGD magnitudes are divided into 2 categories: The DGD magnitudes are divided into 2 categories: $G_2$ ($TE_{0,1}$/$OAM^{\pm}_{\pm1,1}$/$TM_{0,1}$) increases slowly with wavelength valuing around 30 (ps/m). On the other hand, the DGD of $G_3$ ($OAM^{\mp}_{\pm2,1}$,$OAM^{\pm}_{\pm2,1}$) decreases with wavelength and lies in the range (50 to 55 ps/m) exhibiting negative slope. Concerning the effect of $\alpha$, the DGD of $G_2$ slowly increases with $\alpha$, while it decreases with $\alpha$ for $G_3$. The behavior of DGD curves in $G_3$ is explained by the large intermodal separation between $G_3$ ($OAM^{\mp}_{\pm2,1}$,$OAM^{\pm}_{\pm2,1}$) and the fundamental $OAM_{0,1}$ ($\geq 10^{-2}$), in addition to the close proximity of $G_3$ to the cutoff refractive index (i.e. cladding). Even though these results differ from some reported FMF [32] (0 ps/km), [33] (27.5 ps/km) or MMF [28] ($\approx$ 6 ps/m), they are consistent with other reported fibers such as in [12] (27 ps/m) and [18] ($\approx$ 30 ps/m).

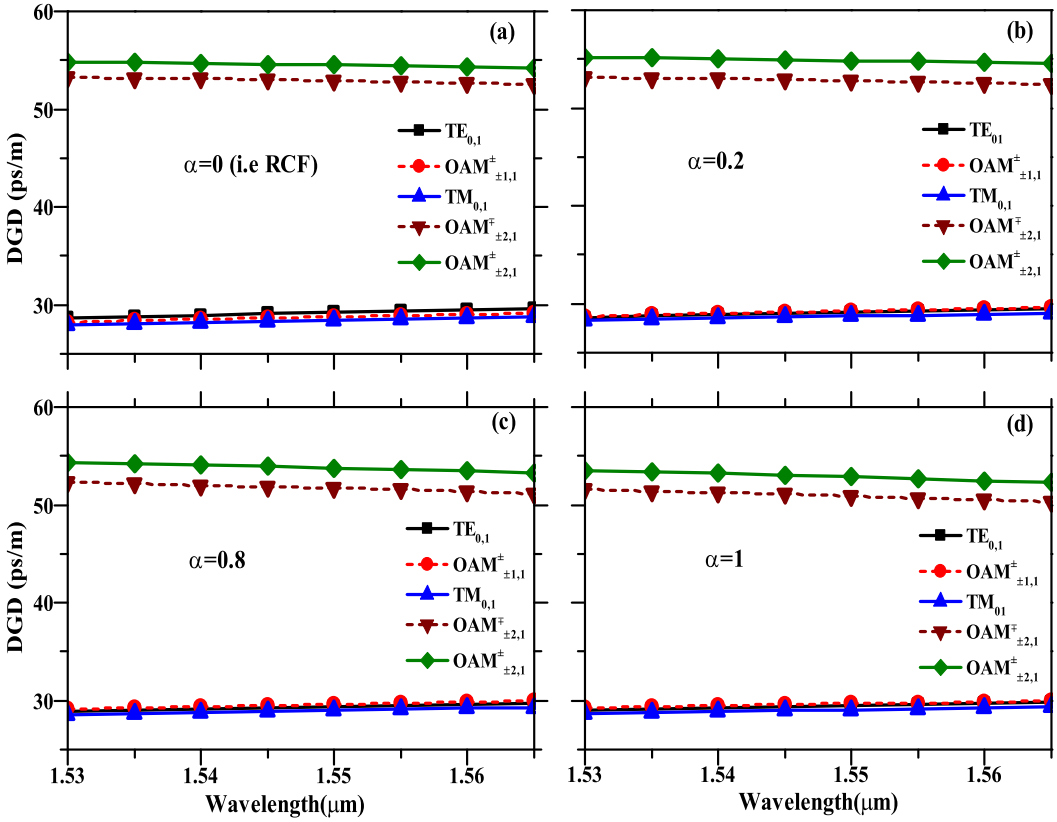


**FIGURE 13.** The Differential group delay of modes (neglecting polarization degenerate modes) of the designed HTAN across the C band for different values of $\alpha$: (a) $\alpha = 0$, (b) $\alpha = 0.2$, (c) $\alpha = 0.8$, and (d) $\alpha = 1$.

## VI. FIBER TOLERANCE TO BENDING

In view of practical uses (environment) of the optical fibers, the fiber is susceptible to perturbations such as bending and twisting. Bent fibers can affect seriously the transmission operation including the intermodal separation, the purity of OAM modes and power loss [34], [35]. After analyzing the unperturbed HTAN fiber, in this section, we examine (investigate) the immunity of the proposed fiber when it is subjected to bend. We study the impacts of fiber bends on the performance of OAM modes. The latter includes the intermodal separation (i.e. Crosstalk), the intra-mode walk-off effect of OAM modes, and the confinement losses of supported modes induced by tighter bending radius ($Rb$) ranging from 2 $mm$ to 25 $mm$. Other fiber parameters are kept as: $a = 3\mu m$, $n_2 = 1.444$, $\Delta n_{max}$=0.05, $n_2 = 1.454$ and $\lambda = 1.55\mu m$. According to the standard conformal mapping approach [35], the straight fiber and bent fiber refractive indexes are linked by the following expression:

$$n_{eq}(x, y) = n(x, y)(1 + \frac{x}{1.40Rb}) \quad (9)$$

where $n(x, y)$ and $n_{eq}(x, y)$ are the straight fiber refractive index and the equivalent bent fiber refractive index, respectively. $Rb$ is the bend radius applied along the transverse x-axis direction. The additional term 1.40, located in denominator, denotes the photoelastic effects on the refractive index induced by the local strain in bent fused silica fibers [36]. By implementing the expression (6) into FEM, we numerically compute the bending effects on modes and address the robustness of such fiber against fiber bend.

### A. INTER-CHANNELS CROSSTALK

Figure 14 illustrates the intermodal separation ($\Delta n_{eff}$) between successive modes as a function of bending radius and for different values of shape parameter $\alpha$. Note here that the supported modes number is the first parameter that is affected by the bending. The higher modes tend to leak out from the core into the cladding (unguided). In HTAN, only at $Rb = 8\ mm$, the fiber supports all the 10 modes presented in straight case. From Figure 14 (a-d), one can see that even under tight bend radius, the intermodal separation remains $> 10^{-4}$ enabling low-level induced channels crosstalk. Hence, HTAN features stronger resilience (tolerance) to fiber bending effect.

### B. MODES WALK OFFS

In addition to the effects on the intermodal separation, fiber bending affects the separation between even and odd modes that form OAM modes, which gives mode walk-off upon propagation. In order to characterize the intra-mode walk-off effect of OAM modes against the fiber bend radius, we calculate the $2\pi$ and 10-ps walk offs lengths ($L_{2\pi}$, $L_{10ps}$) for all the OAM modes in HTAN fiber (for different values of $\alpha$). $L_{2\pi}$ is defined as the propagation length when the even

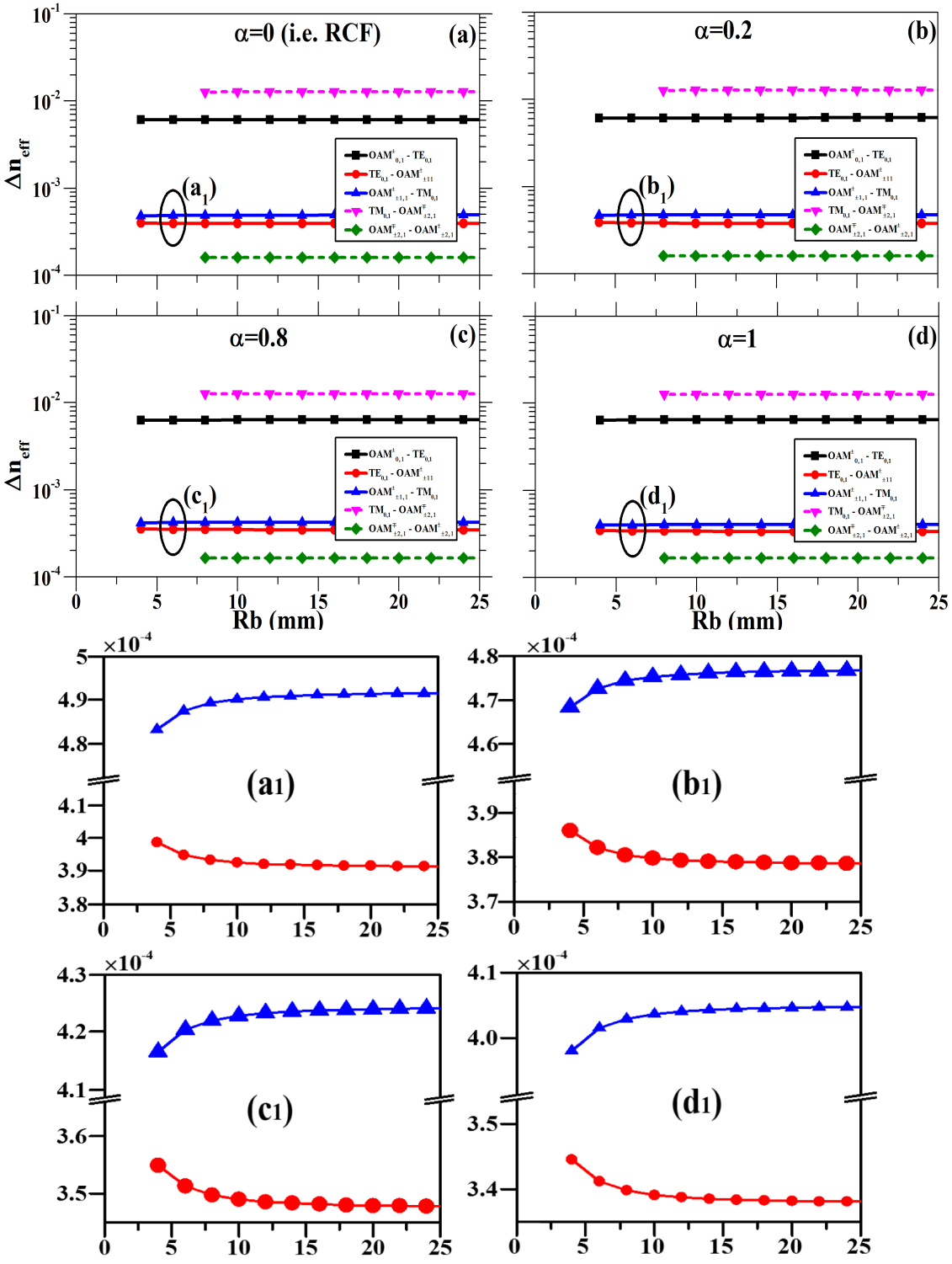


**FIGURE 14.** Intermodal separation versus bending radius and for different values of shape parameter $\alpha$. (a) $\alpha = 0$, (b) $\alpha = 0.2$, (c) $\alpha = 0.8$, and (d) $\alpha = 1$. the zoomed parts: ($a_1$, $b_1$, $c_1$ and $d_1$).

and odd fiber eigenmodes walk off to each other with a relative phase shift of $2\pi$, while $L_{10ps}$ presents the propagation length after the two eigenmodes has a 10-ps temporal walk off.it characterizes the impact of temporal walk-off on the signal quality. Note here that, for 10-Gbaud/s signals, 10-ps temporal walk-off corresponds to 10% of the symbol period [34]. $L_{2\pi}$, $L_{10ps}$ are given as follows:

$$L_{2\pi} = \frac{\lambda}{n_{eff}^{even} - n_{eff}^{odd}} \tag{10}$$

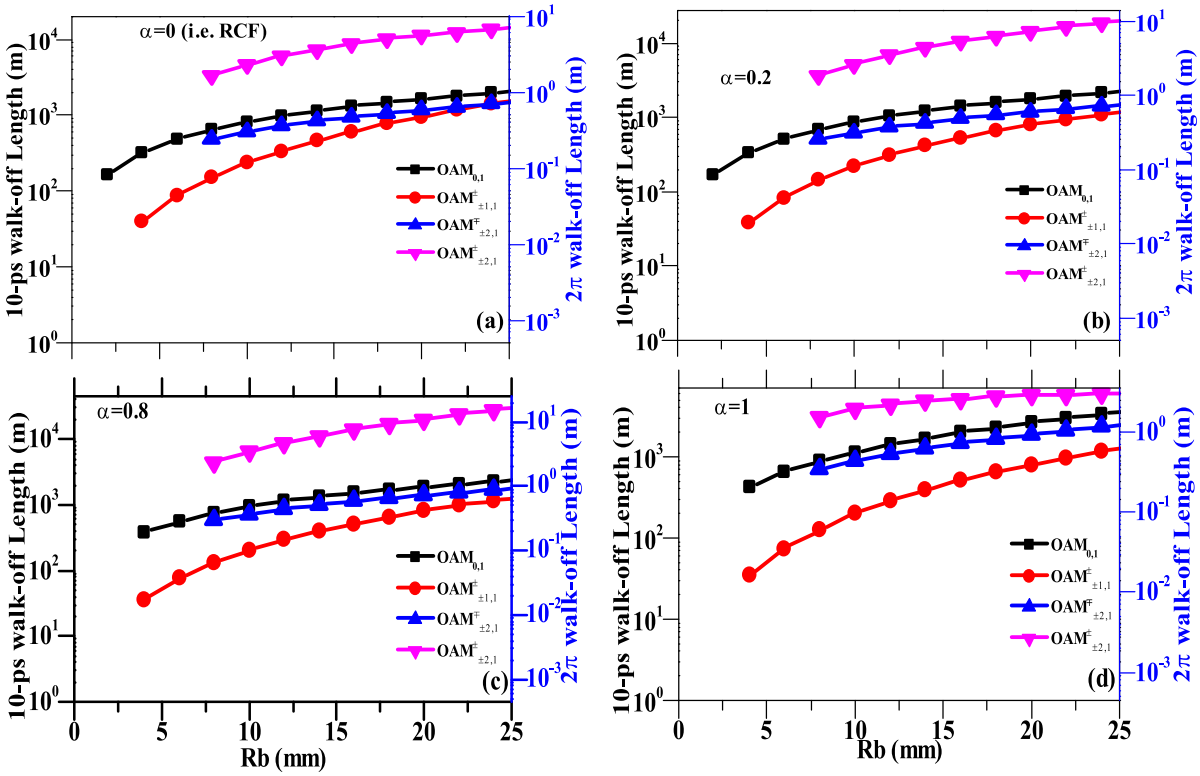


**FIGURE 15.** 10ps walk-off length (m) and 2$\pi$ walk-off length (m) (odd and even) versus bending radius for different values of shape parameter $\alpha$. (a) $\alpha = 0$, (b) $\alpha = 0.2$, (c) $\alpha = 0.8$, and (d) $\alpha = 1$.

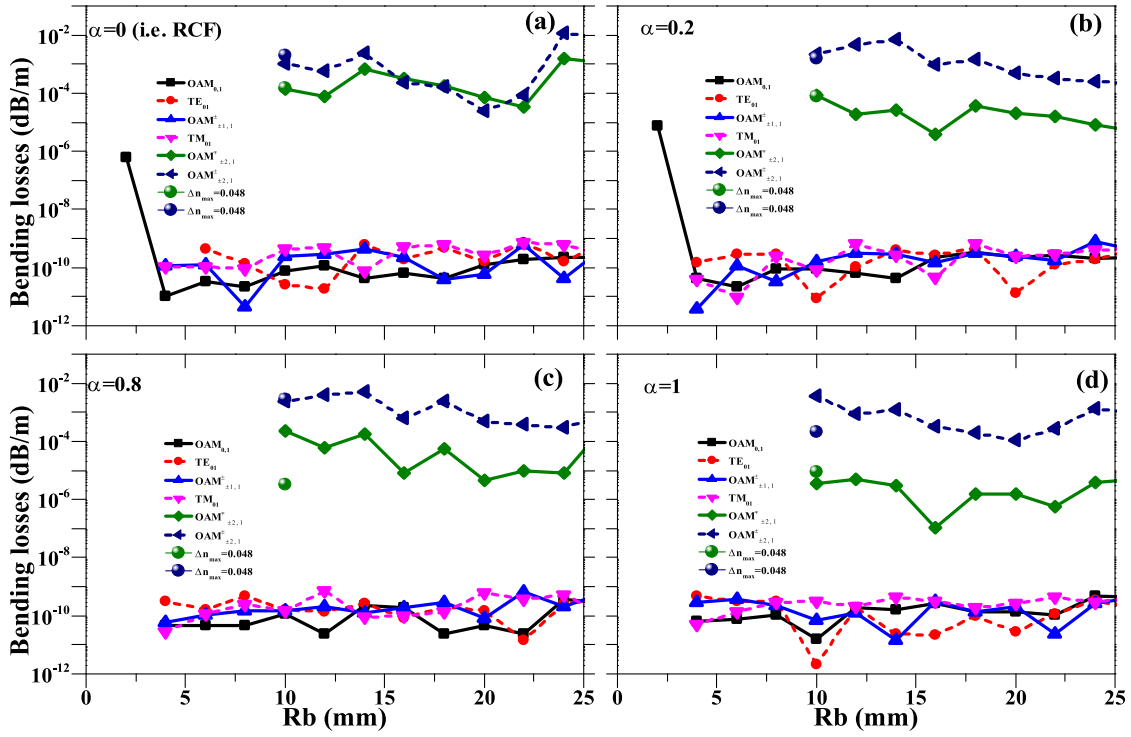


**FIGURE 16.** Confinement losses of supported modes versus bending radius and for different values of shape parameter $\alpha$.(a) $\alpha = 0$, (b) $\alpha = 0.2$, (d) $\alpha = 0.8$, and (d) $\alpha = 1$.

$$L_{10ps} = \frac{c \times \Delta t}{n_{eff}^{even} - n_{eff}^{odd}} \tag{11}$$

where $\lambda$, $c$, and $\Delta t$ are the wavelength, speed of light in a vacuum, and walk-off time ($\Delta t = 10\ ps$), respectively. The

results are shown in Figure 15 (a-d). One can see that $L_{2\pi}$ and $L_{10ps}$ of OAM modes increase exponentially with bending radius. $HE_{3,1}$ related OAM mode has longer $L_{2\pi}$ and $L_{10ps}$, hence smaller effective index separation between even and odd modes, which means that it has more azimuthal periods in its transverse field distribution. Regarding the effect of $\alpha$, ($L_{2\pi}$, $L_{10ps}$) slowly decrease with $\alpha$. The minimum $L_{10ps}$ at $\alpha = 1$ is around 200 km even under tight bend $Rb = 1$ *cm*.These values are reasonable since they are consistent with those recently reported in OAM-fibers in [14], [34].

### C. BENDING LOSS

At last, the bend induces confinement losses (CL) of supported modes. The results are shown in Figure 16 (a-d), where the confinement losses are computed versus $Rb$ and for different values of $\alpha$. We add also the CL of both higher modes at $Rb = 1$ *cm* for $\Delta n_{\max} = 0.048$. From that figure, one can see that higher modes ($EH_{1,1}$ and $HE_{3,1}$ related OAM modes) achieve larger confinement losses due to the proximity to the cut-off (high susceptibility to leak out from the core into the cladding). In contrast, lower modes observe strong modal confinement within the core even under tight bending radius (below $10^{-10}$ (consistent with [38]) ($Rb = 1cm$). Even though it is well known that high index contrast at the core cladding boundary raises the fiber loss, HTAN with the selected parameters shows great bending insensitivity that prevents the addressing of additional complex structure (e.g. by adding trench [39]) to original profile structure. The obtained results are reasonable and in full agreement with those in IPGI [21]. Regarding the effect of bend with parameter $\alpha$, the CL slowly decreases as $\alpha$ increases.

## VII. CONCLUSION

In this work, we have proposed a novel kind of refractive index profile for few mode fiber referred to as a hyperbolic tangent FMF (HTAN-FMF) that could be a good candidate for next generation cylindrical vector modes as well as OAM modes based MDM systems. By performing a theoretical/numerical analysis, we identify the design (key parameters & values) that provide optimized $\Delta n_{\text{eff}}$ among vector modes. These parameters include core radius ($a = 3\mu m$), index contrasts ($\Delta n_{max} = 0.05$, $\Delta n = 0.01$) and shape parameter ($\alpha = 1$). The results show that the optimized $\Delta n_{\text{eff}}$ outperforms what is existing in the literature and enables low crosstalk among channels carrying data during propagation. In addition, the simulations shows that the HTAN-FMF structure complexity (inner smooth & outer sharpe) enhances the purity of synthesized OAM leading to reduced intrinsic crosstalk. Hence, this makes the proposed fiber suitable for next generation long distance OAM fiber. Furthermore, the propagation performance metrics in terms of chromatic dispersion (CD) and differential mode delay (DGD) are examined (across the C ITU-T band) and discussed. The obtained results (max CD = -60 ps/(km.nm), max DGD=55 ps/m) show that HTAN-FMF can be a viable candidate for long distance OAM-MDM based communication. Even under practical condition (bending), the proposed HTAN-FMF shows great insensitivity to bending effects.

In future work, we aim to deeply examine the new profile including the sensitivity to further fiber perturbations such as core ellipticity and fiber twisting and the inter group/core crosstalk in multimode/multicore fiber scenario involving HTAN. The results of such investigation may encourage the industry to prototype the proposed HTAN design.

## APPENDIX I: INTERMODAL SEPARATION: ANALYTICAL APPROACH

The effective index $n_{\text{eff}}$ and the propagation constant $\beta$ of a given vector mode are linked with its scalar degenerate counterpart ($\widetilde{n_{\text{eff}}}$) and ($\widetilde{\beta}$) by the following expressions [21], [27]:

$$n_{eff} = \widetilde{n_{eff}}\sqrt{1 + \delta\beta^2/k_0^2 * \widetilde{n_{eff}}} \;\; and \;\; \beta = \widetilde{\beta}\sqrt{1 + \delta\beta^2/\widetilde{\beta}} \tag{A.12}$$

where $\delta\beta^2$ expresses the applied correction factor lifting the degeneracy of vector modes, $k_0$ is the wave number given by $2\pi/\lambda$. If we neglect the longitudinal component of mode field ($e_z\hat{z}$), the transverse field of a given vector mode is presented as $\overrightarrow{e} = [\hat{e}_r\hat{r}, \hat{e_\varphi}\hat{\varphi}]$ in cylindrical coordinates. The correction factor $\delta\beta^2$ is linked with $\overrightarrow{e}$ by [21], [27]:

$$\delta\beta^2 \approx \frac{-\int \overrightarrow{\nabla}.\overrightarrow{e}.(\overrightarrow{\nabla}.\overrightarrow{e})(ln(n^2))dA}{\int \left|\overrightarrow{e}\right|^2 dA} \tag{A.13}$$

$\overrightarrow{\nabla}$ is the gradient operator, and $n$ is the refractive index function. As reported in [21], the expression A.13 is general and exact for any refractive index profile. The intermodal separation is proportional to $\delta\beta^2$ [15]. Since the proposed HTAN−FMF presents a circular symmetric (the index depends only on $r$), the gradient expressions (of refractive index and mode field are expressed in cylindrical coordinates as [27]:

$$\overrightarrow{\nabla}.(ln(n^2)) = \frac{\widehat{r}}{n(r)^2} \times \frac{dn(r)^2}{dr} \tag{A.14}$$

$$\overrightarrow{\nabla}.\overrightarrow{e} = \frac{1}{r} \times (\frac{\partial(r.er)}{\partial r} + \frac{(\partial e\varphi)}{\partial\varphi}) \tag{A.15}$$

Applying the expression (A.14) on HTAN refractive index distribution (core region), we have:

$$\begin{aligned}
&\overrightarrow{\nabla}.(ln(n_{\text{HTAN}}^2)) \\
&= \frac{\widehat{r}}{n_{\text{HTAN}}(r)^2} \times \frac{dn_{\text{HTAN}}^2}{dr} \\
&= \frac{1}{(\frac{n_1+n_2}{2} + \frac{n_1-n_2}{2tanh(\pi)}tanh(\frac{\pi(r-a_1)}{a_1\alpha}))^2} \\
&\quad \times \frac{d}{dr}(\frac{n_1+n_2}{2} + \frac{n_1-n_2}{2tanh(\pi)}Tanh(\frac{\pi(r-a_1)}{a_1\alpha}))^2
\end{aligned} \tag{A.16}$$

In order to facilitate the analysis, we define $X = [\pi(r - a_1)]/(a_1\alpha)$, and since $\frac{dtanh(X)}{dr} = \frac{\pi}{a_1\times\alpha}(1 - tanh(X)^2)$, the expression (A.16) is written as:

$$\left|\overrightarrow{\nabla}.(ln(n^2))\right| = \frac{\Delta n}{(\frac{n1+n2}{2} + \frac{n1-n2}{2\times tanh(\pi)} \times tanh(\frac{\pi(r-a_1)}{a_1\times\alpha}))^2} \times 2 \times (\frac{\pi\,\Delta n}{2 \times a_1 \times \alpha \times tanh(\pi)} \times (1 - tanh(X)^2)) \times (\frac{n_1 + n_2}{2} + \frac{\Delta n}{2 \times tanh(\pi)} \times tanh(X)) \tag{A.17}$$

which is then simplified and expressed as:

$$\begin{aligned}\left|\overrightarrow{\nabla}.(ln(n^2))\right| &= \frac{\frac{\pi\times\Delta n}{a_1\times\alpha\times tanh(\pi)} \times (1 - tanh(X)^2)}{\frac{n1+n2}{2} + \frac{\Delta n}{2\times tanh(\pi)} \times tanh(\pi)} \\ &= \frac{2 \times \pi \times \Delta n \times (1 - tanh(X)^2)}{a_1 \times \alpha \times (tanh(\pi) \times (n_1 + n_2) + \Delta n \times tanh(X))}\end{aligned} \tag{A.18}$$

Evaluating the resulting expression at the bound $a\frac{(1+\alpha)}{2}$, we find the following proportionality relation:

$$\left|\overrightarrow{\nabla}.(ln(n^2))\right| \propto \frac{\Delta n}{\alpha a n_1} \tag{A.19}$$

## ACKNOWLEDGMENT

This work was supported by the Researchers Supporting Project number (RSP-2020/46), King Saud University, Riyadh, Saudi Arabia.

## REFERENCES

[1] *Cisco Global Cloud Index: Forecast and Methodology, 2015-2020*, Cisco, San Jose, CA, USA, 2020.
[2] L. A. Rusch, M. Rad, K. Allahverdyan, I. Fazal, and E. Bernier, "Carrying data on the orbital angular momentum of light," *IEEE Commun. Mag.*, vol. 56, no. 2, pp. 219–224, Feb. 2018.
[3] D. J. Richardson, J. M. Fini, and L. E. Nelson, "Space-division multiplexing in optical fibres," *Nature Photon.*, vol. 7, no. 5, p. 354–362, 2013.
[4] R. Ryf, S. Randel, A. H. Gnauck, C. Bolle, A. Sierra, and S. D. W. M. Peckham, "Mode-division multiplexing over 96 km of few-mode fiber using coherent 6 × 6 MIMO processing," *J. Lightw. Technol.*, vol. 30, no. 4, pp. 521–531, 2012.
[5] R. Ryf *et al.*, "12 × 12 MIMO transmission over 130-km few-mode fiber," in *Frontiers in Optics*. Washington, DC, USA: OSA, Oct. 2012, p. FW6C-4.
[6] A. M. Yao and M. J. Padgett, "Orbital angular momentum: Origins, behavior and applications," *Adv. Opt. Photon.*, vol. 3, no. 2, pp. 161–204, Jun. 2011.
[7] J. Wang, S. Li, M. Luo, J. Liu, L. Zhu, C. Li, D. Xie, Q. Yang, S. Yu, J. Sun, and X. Zhang, "N-Dimentional multiplexing link with 1.036-Pbit/s transmission capacity and 112.6-bit/s/Hz spectral efficiency using OFDM-8 QAM signals over 368 WDM pol muxed 26 OAM modes," In *Proc. 40th Eur. Conf. Opt. Commun.*, Cannes, France. Piscataway, NJ, USA: IEEE, Sep. 2014, Paper Mo.4.5.1.
[8] B. B. Yousif and E. E. Elsayed, "Performance enhancement of an Orbital-Angular-Momentum-Multiplexed free-space optical link under atmospheric turbulence effects using spatial-mode multiplexing and hybrid diversity based on adaptive MIMO equalization," *IEEE Access*, vol. 7, pp. 84401–84412, 2019.
[9] S. Ramachandran, P. Kristensen, and M. F. Yan, "Generation and propagation of radially polarized beams in optical fibers," *Opt. Lett.*, vol. 34, pp. 2525–2527, Aug. 2009.
[10] N. Bozinovic, Y. Yue, Y. Ren, M. Tur, P. Kristensen, H. Huang, A. E. Willner, and S. Ramachandran, "Terabit-scale orbital angular momentum mode division multiplexing in fibers," *Science*, vol. 340, pp. 1545–1548, Jun. 2013.
[11] P. Gregg, P. Kristensen, S. E. Golowich, J. ø. Olsen, P. Steinvurzel, and S. Ramachandran, "Stable transmission of 12 OAM states in air-core fiber," in *Proc. CLEO*, 2013, pp. 1–2, Paper CTu2K2.
[12] C. Brunet, P. Vaity, Y. Messaddeq, S. LaRochelle, and L. A. Rusch, "Design, fabrication and validation of an OAM fiber supporting 36 states," *Opt. Exp.*, vol. 22, no. 21, pp. 26117–26127, 2014.
[13] K. Ingerslev, P. Gregg, M. Galili, F. Da Ros, H. Hu, F. Bao, M. A. U. Castaneda, P. Kristensen, A. Rubano, L. Marrucci, and K. Rottwitt, "12 mode, WDM, MIMO-free orbital angular momentum transmission," *Opt. Exp.*, vol. 26, pp. 20225–20232, Aug. 2018.
[14] Y Wang, C. Bao, W. Geng, Y. Lu, Y. Fang, B. Mao, Y.-G. Liu, H. Huang, Y. Ren, and Z. Pan, "Air-core ring fiber with >1000 radially fundamental OAM modes across O, E, S, C, and L bands," *IEEE Access*, vol. 8, pp. 68280–68287, 2020.
[15] C. Brunet, B. Ung, P.-A. Bélanger, Y. Messaddeq, S. LaRochelle, and L. A. Rusch, "Vector mode analysis of ring-core fibers: Design tools for spatial division multiplexing," *J. Lightw. Technol.*, vol. 32, no. 23, pp. 4046–4057, 2014.
[16] S. Chen, S. Li, L. Fang, A. Wang, and J. Wang, "OAM mode multiplexing in weakly guiding ring-core fiber with simplified MIMO-DSP," *Opt. Exp.*, vol. 27, no. 26, pp. 38049–38060, 2019.
[17] R. Zhang, H. Tan, J. Zhang, L. Shen, J. Liu, Y. Liu, L. Zhang, and S. Yu, "A novel ring-core fiber supporting MIMO-free 50 km transmission over high-order OAM modes," in *Proc. Opt. Fiber Commun. Conf. (OFC)*, 2019, pp. 1–3.
[18] G. Zhu, Z. Hu, X. Wu, C. Du, W. Luo, Y. Chen, X. Cai, J. Liu, J. Zhu, and S. Yu, "Scalable mode division multiplexed transmission over a 10-km ring-core fiber using high-order orbital angular momentum modes," *Opt. Exp.*, vol. 26, no. 2, pp. 594–604, 2018.
[19] L. Zhu, G. Zhu, A. Wang, L. Wang, J. Ai, S. Chen, C. Du, J. Liu, S. Yu, and J. Wang, "18 km low-crosstalk OAM + WDM transmission with 224 individual channels enabled by a ring-core fiber with large high-order mode group separation," *Opt. Lett.*, vol. 43, no. 8, pp. 1890–1893, Apr. 2018.
[20] A. Rjeb, G. Guerra, K. Issa, H. Fathallah, S. Chebaane, M. Machhout, L. Palmieri, and A. Galtarossa, "Inverse-raised-cosine fibers for next-generation orbital angular momentum systems," *Opt. Commun.*, vol. 458, Mar. 2020, Art. no. 124736.
[21] B. Ung, P. Vaity, L. Wang, Y. Messaddeq, L. A. Rusch, and S. LaRochelle, "Few-mode fiber with inverse-parabolic graded-index profile for transmission of OAM-carrying modes," *Opt. Exp.*, vol. 22, no. 15, pp. 18044–18055, Jul. 2014.
[22] X. Wang, S. Yan, J. Zhu, Y. Ou, Z. Hu, Y. Messaddeq, S. LaRochelle, L. A. Rusch, D. Simeonidou, and S. Yu, "3.36-Tbit/s OAM and wavelength multiplexed transmission over an inverse-parabolic graded index fiber," in *Proc. Conf. Lasers Electro-Opt.*, San Jose, CA, USA, May 2017, Paper SW4I.3.
[23] T. Yang, Y. Wei, Z. Tu, H. Zeng, M. A. Kinsy, N. Zheng, and P. Ren, "Design space exploration of neural network activation function circuits," *IEEE Trans. Comput.-Aided Design Integr. Circuits Syst.*, vol. 38, no. 10, pp. 1974–1978, Oct. 2019.
[24] G. Garg and P. Sharma, "An analysis of contrast enhancement using activation functions," *Int. J. Hybrid Inf. Technol.*, vol. 7, no. 5, pp. 235–244, Sep. 2014.
[25] H. K. Johansen and K. Sørensen, "Fast Hankel transforms," *Geophys. Prospecting*, vol. 27, no. 4, pp. 876–901, Dec. 1979.
[26] A. Goyal and H. M. Kwon, "Hyperbolic tangent function avoided for encoded pilot low density parity check decoding," in *Proc. Eur. Conf. Wireless Technol.*, Oct. 2005, pp. 149–152.
[27] L. J. Bures, *Guided Optics: Optical Fibers and All-Fiber Components*. Hoboken, NJ, USA: Wiley, 2009, ch. 5.
[28] H. Doweidar, "Considerations on the structure and physical properties of $B_2O_3$–$SiO_2$ and $GeO_2$–$SiO_2$ glasses," *J. Non-Cryst. Solids*, vol. 357, no. 7, p. 1665–1670, 2011.
[29] S. Chen and J. Wang, "Theoretical analyses on orbital angular momentum modes in conventional graded-index multimode fibre," *Sci. Rep.*, vol. 7, no. 1, p. 3990, Dec. 2017.

[30] Z. Zhang, J. Gan, X. Heng, Y. Wu, Q. Li, Q. Qian, and Y. Zamp, "Optical fiber design with orbital angular momentum light purity higher than 99.9%," *Opt. Exp.*, vol. 23, no. 23, pp. 29331–29341, Nov. 2015.
[31] P. Gregg, P. Kristensen, and S. Ramachandran, "13.4 km OAM state propagation by recirculating fiber loop," *Opt. Exp.*, vol. 24, no. 17, pp. 18938–18947, 2016.
[32] S. Chebaane, H. Fathallah, H. Seleem, and M. Machhout, "Proposed raised cosine FMF for dispersion management in next-generation optical networks," *IEEE Photon. J.*, vol. 8, no. 1, pp. 1–6, Feb. 2016.
[33] J. Zhao, B. Li, M. Tang, S. Fu, P. P. Shum, and D. Liu, "Hole-assisted graded-index four-LP-mode fiber with low differential mode group delay over C+L band," *IEEE Photon. J.*, vol. 8, no. 6, pp. 1–10, Dec. 2016.
[34] S. Li and J. Wang, "A compact trench-assisted multi-orbital-angular-momentum multi-ring fiber for ultrahigh-density space-division multiplexing (19 rings × 22 Modes)," *Sci. Rep.*, vol. 4, no. 1, May 2015.
[35] M. Heiblum and J. Harris, "Analysis of curved optical waveguides by conformal transformation," *IEEE J. Quantum Electron.*, vol. 11, no. 2, pp. 75–83, Feb. 1975.
[36] C. Schulze, A. Lorenz, D. Flamm, A. Hartung, S. Schröter, H. Bartelt, and M. Duparré, "Mode resolved bend loss in few-mode optical fibers," *Opt. Exp.*, vol. 21, no. 3, pp. 3170–3181, 2013.
[37] Y. Yue, Y. Yan, N. Ahmed, J. Y. Yang, L. Zhang, Y. Ren, H. Huang, K. M. Birnbaum, B. I. Erkmen, S. Dolinar, and M. Tur, "Mode properties and propagation effects of optical orbital angular momentum (OAM) modes in a ring fiber," *IEEE Photon. J.*, vol. 4, no. 2, pp. 535–543, Apr. 2012.
[38] I. J. Lee, J. Song, and S. Kim, "Analysis of bending-induced degradation of orbital angular momentum modes in optical fibers," *Photonics*, vol. 6, no. 3, p. 97, Sep. 2019.
[39] P. R. Watekar, S. Ju, and W. T. Han, "Design and development of a trenched optical fiber with ultra-low bending loss," *Opt. Exp.*, vol. 17, no. 12, pp. 10350–10363, 2009.

**ALAAEDDINE RJEB** received the B.Sc. degree (Hons.) in physics from the University of Monastir, Tunisia, in 2014, and the M.A. degree (Hons.) in electronics and microelectronics from the Faculty of Sciences, University of Monastir, in December 2016, where he is currently pursuing the Ph.D. degree with the Electronics and Microelectronics Lab, Department of Physics, under the supervision of Prof. Habib Fathallah and co-supervision of Prof. Mohsen Machhout. From January 2017 to September 2017, he was a Research Fellow with the Electronics and Microelectronics Lab, Department of Physics, University of Monastir. His main Ph.D. topic is about few mode-optical fiber designs with focus on next generation orbital angular momentum specialty fiber. He is currently a Contractual Assistant with Technology Department, Higher Institute of Computer Sciences and Mathematics of Monastir (ISIMM). His research and teaching interests include next generation networks (NGN), micro and nano electronics devices, data and network security (DNS), the Internet of Things (IOT) and smart systems, machine learning, and big data.

**HABIB A. FATHALLAH** (Senior Member, IEEE) received the B.S.E.E degree (with Hons.) from the National Engineering School of Tunis, in 1994, and the M.A. and Ph.D. degrees in electrical and computer engineering from Laval University, Canada, in 1997 and 2001, respectively. He holds several teaching and research positions in Electrical and Computer Engineering with Laval University, King Saud University (KSA), and Carthage University, Tunisia. He was the Founder and the CEO of Access Photonic Networks, from 2001 to 2006 and the Co-Founder of KACST-Technology Innovation Center for the e-Society, from 2010 to 2017. His actual research interests include next generation networks and virtualization, the Internet of Things and Vehicles, queuing theory and smart systems, and stochastic and probabilistic modeling.

**ISSA KHALED** received the B.Sc. degree (Hons.) from the Preparatory Institute of Scientific and Technical Studies (IPEST), Tunisia, in 2006, and the M.Sc. degree in physics and the Ph.D. degree (Hons.) from the Faculty of Science Monastir, Tunisia, in 2008 and 2016, respectively. He was an Electro-Optic Research Engineer with IPEST and the Institute of Nanotechnology of Lyon (INL), France, and the Laser Center Jussieu, Université Pierre et Marie Curie, France, from 2004 to 2006. He was a Photonic Engineer with INL, from 2008 to 2009. He was a Teacher Assistant with the Faculty of Science of Monastir, from 2008 to 2014. His main research interests include the atomic, molecular interaction and systems, advanced quantum studies, and rare gas clusters. He joined as a Researcher with KACST-RFTONICS, KSU, in 2014. He has authored, presented, and submitted peer reviewed conferences and journal papers. He has supervised undergraduate student's projects in optical telecommunication and renewable energy areas. He co-supervised graduate students. He mainly involved on antenna analysis, synthesis and characterization projects, nano-fabrication and nano characterization of nano-structures, and various funded research projects by NSTIP and RFTONICS-TIC.

**MOHSEN MACHHOUT** was born in Jerba, in January 1966. He received the M.S. and Ph.D. degrees in electrical engineering from the University of Tunis II, Tunisia, in 1994 and 2000, respectively. He is currently a Professor with the University of Monastir, Tunisia, where he is also the Director of the Electronics and Microelectronics Laboratory, Department of Physics. He has authored more than 100 publications. His research interests include the implementation of standard cryptography algorithm, key stream generator and electronic signature on FPGA and ASIC, security of smart card, and embedded systems with resource constraints.

**SALEH A. ALSHEBEILI** (Member, IEEE) was the Chairman of the Electrical Engineering Department, King Saud University, from 2001 to 2005. He has more than 27 years of teaching and research experience in the area of communications and signal processing. He was a member of the Board of Directors with the King Abdullah Institute for Research and Consulting Studies, from 2007 to 2009, and a member of the Board of Directors with the Prince Sultan Advanced Technologies Research Institute, from 2008 to 2017, where he was the Managing Director from 2008 to 2011 and the Director of the Saudi-Telecom Research Chair from 2008 to 2012. He has been the Director of the Technology Innovation Center, RF and Photonics in the E-Society, funded by the King Abdulaziz City for Science and Technology (KACST), since 2011. He is currently a Professor with the Electrical Engineering Department, King Saud University. He has been on the Editorial Board of the *Journal of Engineering Sciences* of King Saud University from 2009 to 2012. He has also an active involvement in the review process of a number of research journals, KACST general directorate grants programs, and national and international symposiums and conferences.